Palaeogeography, Palaeoclimatology, Palaeoecology 378 (2013) 75–90

Contents lists available at SciVerse ScienceDirect

Palaeogeography, Palaeoclimatology, Palaeoecology

journal homepage: www.elsevier.com/locate/palaeo

Testing high resolution magnetic susceptibility and gamma radiation methods in the Cenomanian–Turonian (Upper Cretaceous) GSSP and near-by coeval section

Brooks B. Ellwood [a,*], Wei-Hsung Wang [b], Jonathan H. Tomkin [c], Kenneth T. Ratcliffe [d], Ahmed El Hassani [e], Amelia M. Wright [d]

[a] Louisiana State University, Department of Geology and Geophysics, E235 Howe-Russell Geoscience Complex, Baton Rouge, LA 70803, USA
[b] Louisiana State University, Center for Energy Studies, 112 Nuclear Science Building, Baton Rouge, LA 70803, USA
[c] School of Earth, Society, and Environment, University of Illinois, 428 Natural History Building, 1301 W. Green Street, Urbana, IL 61801, USA
[d] Chemostrat Inc., 5850 San Felipe, Suite 500, Houston, 77057, USA
[e] Institut Scientifique, Université Mohammed V Agdal, B.P.703 Rabat-Agdal, 10106 Rabat, Morocco

ARTICLE INFO

Article history:
Received 8 October 2011
Received in revised form 15 February 2013
Accepted 18 February 2013
Available online 13 March 2013

Keywords:
Magnetic susceptibility (χ)
Gamma radiation spectroscopy (GRS)
^{40}K
Cenomanian–Turonian GSSP
Instrumental evaluation
High resolution time-series analysis

ABSTRACT

Low-field, mass specific magnetic susceptibility (χ) and gamma radiation spectra (GRS) field and laboratory data sets for two Upper Cretaceous marine sedimentary sequences representing the Cenomanian–Turonian (C–T) boundary in the Western Interior Seaway in central Colorado have been measured, sections including the C–T Global boundary Stratotype Section and Point (GSSP) and a ~one kilometer distant co-eval sequence, the S Section. It has previously been established that both χ and GRS data sets are controlled by detrital/eolian fluxes into the marine environment, although the effect of weathering, if any, on these parameters when exposed in outcrop, is not well documented. In addition, these parameters are controlled by differing detrital/eolian components that may be derived from different sources, or be differentially concentrated within the marine system. Of great interest is (1) how well these data sets record climate cycles, (2) how the χ and GRS data are affected by weathering, and (3) how well the two methods support each other. Reported here are the results of a number of field and laboratory experiments designed to evaluate instruments and how χ and GRS data sets co-vary, and to test their usefulness as correlation tools in stratigraphy. Results show that both χ and ^{40}K data sets from laboratory measurement on samples collected in the field, where rocks are relatively fresh, are generally well correlated, respond closely to climate and the corresponding detrital/eolian flux into the marine environment, and can be used for a rough proxy for each other. However, weathering appears to affect the ^{40}K data by removing ^{40}K, thus reducing correlation potential, although χ does not appear to suffer as badly in more weathered sections and good correlations between sections remain. Field GRS measurements produce a broadly smoothed data set that regionally can be very useful for correlation, although potential global correlations are not tested here. Using χ data reported here, and comparing these data to a ~100 kyr cyclic, eccentricity (E1) climate model for the Upper Cretaceous at ~93.9 Ma, shows that χ and ^{40}K data, measured in the laboratory, can be used to build floating point time scales that produce essentially equivalent results as do other studies using absolute dates.

1. Introduction

The Cenomanian–Turonian (C–T) boundary interval in the Upper Cretaceous has been extensively studied, in part because it is associated with an oceanic environmental disruption that resulted in the development of anoxic or dysoxic bottom waters (Berrocoso et al., 2008; Pearce et al., 2009), causing the extinctions of many organisms (Barnes et al., 1996; Voigt et al., 2004; Kennedy et al., 2005; Parente et al., 2008). This Oceanic Anoxic Event 2 (OAE2; Schlanger and Jenkyns, 1976) was associated with global climatic changes, where both warming and cooling arguments have been made (e.g., Arthur et al., 1988; Huber et al., 1999), and provides data associated with an important climatic event that can potentially help understand the causes of oceanographic changes that are occurring today. The OAE2 climatic event is defined, in part, by a major, positive δ^{13}C anomaly that has been shown to have lasted for as little as 100 kyr (Keller et al., 2004) to as long as 885 kyr (Sageman et al., 2006).

Some work has suggested that OAE2 may have resulted from sub-marine volcanism (Turgeon and Creaser, 2008). It has been argued that enhanced preservation or burial of carbon, the mechanism for producing the large positive δ^{13}C anomaly defining OAE2, may have resulted from a widespread magmatic pulse associated with flood basalts or volcanism associated with sea-floor spreading (Turgeon and Creaser, 2008) and high spreading rates demonstrated to have occurred at that time (Seton et al., 2009). This rapid spreading

* Corresponding author.
E-mail address: ellwood@lsu.edu (B.B. Ellwood).

0031-0182/$ – see front matter © 2013 Elsevier B.V. All rights reserved.
http://dx.doi.org/10.1016/j.palaeo.2013.02.018

event resulted in high sea-level and enhanced continental flooding, along with the development of anoxic deep basin and dysoxic epicontinental water masses (Berrocoso et al., 2008; van Bentum et al., 2009) like those of the Western Interior Seaway where the Global boundary Stratotype Section and Point (GSSP) has been established (Kennedy et al., 2005). Certainly there is evidence through the OAE2 interval at the Pueblo GSSP of active volcanism, but evidence of volcanism is found well above and well below the C–T boundary level, shown by bentonite beds that are identified throughout the region (e.g. Kennedy et al., 2005).

One problem with oxygen-minimum zone (OMZ) studies is the question of resolution and correlation among sites that are actually associated with an OMZ, versus geological times with other apparently similar positive $\delta^{13}C$, such as excursions known to occur through much of Cenomanian time (Jarvis et al., 2001). Furthermore, it is important to precisely correlate geological sections so that small-scale changes in chemistry and biota can be reliably placed in an equivalent time-context. Because the GSSP has been established for the C–T boundary (Kennedy et al., 2005), and many sites were studied during the build-up to the selection of the C–T GSSP in Pueblo, Colorado, there is now a well-studied standard to which other work is being correlated. Numerous papers report data from the GSSP or refer to it, directly or indirectly, in an attempt to correlate back to this standard section (e.g., Voigt et al., 2007; Gale et al., 2008; Elrick et al., 2009), but for many sections, due to a lack of definitive taxa, there are problems correlating directly back to the GSSP (e.g., Forster et al., 2008) and therefore directly to the boundary Point.

For such correlation purposes, abiotic geophysical and geochemical techniques are often employed in stratigraphic studies, some methods being relatively easy to apply, inexpensive and potentially quite useful; while others are, for differing reasons, not as effective. For example, with the right equipment it is quick and cost effective to measure the low-field, mass specific magnetic susceptibility (χ), either on samples collected in the field for that purpose, or directly in the field with portable instruments. This is also true for gamma radiation methods, although field gamma radiation spectroscopy (GRS) and gamma radiation laboratory measurements are fairly time consuming. Results from a number of field-based studies on χ and GRS have been reported (i.e., Hladil et al., 2006; Halgedahl et al., 2009).

There are important questions concerning these types of correlation tools that are not yet fully answered. Are χ and GRS measurements, within single sections or between closely spaced sections, highly correlated and therefore can each independently provide a proxy for the other? Can GRS measurements provide a time-series data set as has been demonstrated for χ measurements (i.e., Weedon et al., 1999)? Do total elemental potassium measurements provide a proxy for ^{40}K measurements and vice-versa?

The purpose of this study was four fold; to evaluate, (1) the combined potential of χ and GRS as a correlation tool using well-studied C–T sequences, (2) the effect of weathering on χ and GRS values, (3) the effect of changing lithologies on χ and GRS values, and (4) the differences between field-based and laboratory-based measurements using χ, GRS, and laboratory ^{40}K data sets. This work includes analysis of the moderately weathered GSSP for the C–T boundary exposed in a railroad cut near Pueblo, CO, and analysis of the nearby (~1 km) coeval S Section, exposed along a roadway in Lake Pueblo State Park (Fig. 1), where weathering is more pronounced.

2. Previous work

2.1. Low-field mass specific magnetostratigraphic susceptibility (χ)

In stratigraphic studies it is relatively easy to measure χ, either on samples collected in the field for that purpose, or directly in the field with portable instruments. All materials are "susceptible" to becoming magnetized in the presence of an external magnetic field, and initial low-field mass specific χ is an indicator of the strength of this transient magnetism. χ is very different from remanent magnetism (RM), the intrinsic magnetization that accounts for the magnetostratigraphic polarity of materials. χ in marine stratigraphic sequences is generally considered to be an indicator of detrital/eolian iron-containing paramagnetic and ferrimagnetic grains, mainly ferromagnesian and clay minerals (Bloemendal and deMenocal, 1989; Ellwood et al., 2000, 2008; da Silva and Boulvain, 2002, 2005), although many compounds that don't contain iron are paramagnetic. χ can be quickly and easily measured on small samples. In the very low inducing alternating magnetic fields that are generally applied, χ is largely a function of the concentration and composition of the magnetizable material in a sample. χ can be measured on small, irregular lithic fragments and on highly friable material that is difficult to sample for RM measurement.

χ results, for almost all studies of marine sedimentary rocks, show many levels of cycles. Some of these cycles are very long-term and are

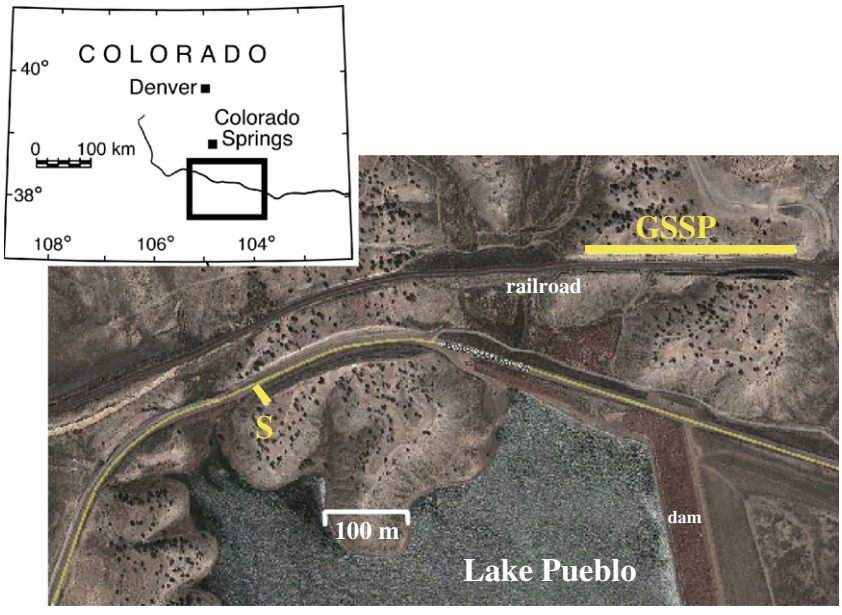

Fig. 1. Location map of the C–T GSSP and S Section at Pueblo, Colorado (Google Earth image).

interpreted as resulting from transgressive–regressive variations (T–R cycles) due to sea level rise and fall associated with eustacy and erosion along continental margins. Other cycles are much shorter and are interpreted to result from climatically driven processes, where cyclic detrital/eolian erosional pulses are responsible for χ variations observed (i.e., Crick et al., 2001; Hladil et al., 2006). Work by da Silva and Boulvain (2005) for Upper Devonian rocks in Belgium has shown a direct, high correlation between 4th order T–R cycles and χ variations determined for the rocks they studied. In addition to these cycles, there are distinct χ peaks that are correlated to maximum flooding surfaces (MFS), and to sudden influxes of detrital/eolian material into sedimentary basins by turbidity currents or other sediment suspensions.

Large magnitude, rapid shifts in χ, represented by multiple data points, are interpreted to result from geological processes that reflect fundamental changes in the sediments being delivered to marine basins. For example, the sharp change from low χ in the Permian to high χ in the Triassic (Hansen et al., 1999) is argued to result from a sudden dramatic influx into ocean basins of detrital/eolian material that helped to cause the mass extinctions in marine fauna at this time (Thoa et al., 2004). A similar pulse in χ is associated with the K–T boundary and is attributed to erosion following the meteorite impact at that time (Ellwood et al., 2003).

As part of this work, χ measurements were made in the field using a Bartington field probe and samples were collected from the same spots and returned to the laboratory for comparison measurements. It is concluded from this work that field measurement using χ techniques has drawbacks. Available instruments have relatively low sensitivity and are very susceptible to anomalous readings because of the small area of material measured and due to other factors. However, such instruments are very useful for rapid field exploration when looking for χ anomalies in outcrop. Many laboratory instruments are much more sensitive and samples collected in the field and brought into the laboratory for measurement can be cleaned and prepared to avoid contaminants.

2.2. Controls on magnetic susceptibility in marine sedimentary rocks

During diagenesis χ in marine sediments decreases. This occurs because ferrimagnetic grains that dominate in unlithified sediments are generally converted to paramagnetic phases during burial and diagenesis, mainly by the action of sulfate reducing bacterial organisms. The result is that within less than a meter of the sediment water interface, new iron minerals, commonly pyrite and siderite, are formed and most ferrimagnetic minerals, such as magnetite and maghemite are destroyed (Karlin and Levi, 1983, 1985; Ellwood et al., 1988). As a result, χ magnitudes are rapidly reduced from values observed in unconsolidated near-surface sediments (Ellwood et al., 2006), to χ values typically ranging from ~1×10^{-9} to 2×10^{-7} m^3/kg (Ellwood et al., 2000). Even where very high sediment accumulation rates are observed, these processes are known to occur (Karlin and Levi, 1985). Very similar results, rapid destruction of ferrimagnetic minerals due to sulfate reducing bacterial organisms, were reported by Ellwood and Burkart (1996) for landfill sediments washed by escaping methane gas generated in the landfill. In general, however, this process does not remove iron from the system, so that total iron content is preserved in new paramagnetic mineral phases. These new phases then contribute, along with the other paramagnetic detrital/eolian components present, and the remaining or authigenic ferrimagnetic constituents, to χ in lithified sediments.

A test of χ variability in single limestone beds has demonstrated the stability of χ over distances up to 25 km (Ellwood et al., 1999). Clear climate cyclicity recorded by χ values indicates that primary climate cycles are preserved in these data sets (i.e. Bloemendal and deMenocal, 1989; Weedon et al., 1999; Jovane et al., 2006; Ellwood et al., 2008). Diagenesis also modifies some of the paramagnetic terrigenous constituents of marine sediments. In many cases clays dominate the detrital/eolian component, and these are generally not destroyed, but may be altered. However, the iron is still conserved in the secondary clays, as is the paramagnetic behavior of these materials.

Many workers use RM measurements to identify minerals contributing to the χ signature in samples, and they conclude from these measurements that χ in marine sediments is dominated by ferrimagnetic components. One difficulty with using such techniques to evaluate if paramagnetic or ferrimagnetic minerals dominate χ is that most remanence techniques only identify ferrimagnetic components in samples, not paramagnetic or diamagnetic components. Because ferrimagnetic constituents are ubiquitous in most natural sedimentary systems, RM methods will 'see' the remanence and miss the contributions of paramagnetic or diamagnetic components. An example of this problem was shown for surface sediments from the Gulf of Mexico (GOM) by Ellwood et al. (2006). In that experiment the authors collected core-top and grab samples from over 200 sites and measured both the anhysteretic remanent magnetism (ARM) and χ. The ARM data show a very symmetrical eastern and western GOM pattern (Fig. 2), whereas χ data show a very asymmetrical pattern, with relatively high χ in the west and very low, diamagnetic or near-diamagnetic χ values associated with the relatively clean carbonate- and quartz-dominated sands along the eastern and southern margins of the GOM. Because there are extremely fine ferrimagnetic particles in all these samples, the ARM shows high values, whereas the χ, dominated by diamagnetic components, shows very low or negative values. The χ signal did not respond to the very fine-grained magnetite present, in part because such extremely small, single domain and pseudo-single domain grains, unless very abundant, tend not to respond to the very low, alternating inducing magnetic fields used in measuring χ.

A second problem with the argument that most marine sediments are dominated by ferrimagnetic components is shown in other experiments by Ellwood et al. (2000). When large blocks of limestone were dissolved and the residue weighed and plotted against χ values for these samples, measured before dissolution, the result showed a well-defined direct relationship between natural χ values and the mass of the residue, the detrital/eolian component in each sample. This relationship was replicated experimentally by using paramagnetic mineral powders diluted in reagent-grade calcium carbonate acting as the 'rock matrix'. However, when powders of rocks that contain a very small amount of ferrimagnetic minerals like magnetite were used, χ values, $\gg 2 \times 10^{-7}$ m^3/kg, were observed to lie well outside the range of normal marine χ, shown to be in the range of 1×10^{-9}–2×10^{-7} m^3/kg (Ellwood et al., 2000). χ in relatively coarse-grained magnetite is extremely high, even in very small amounts. Therefore, to produce normal χ values for lithified marine sedimentary rocks containing abundant diamagnetic and paramagnetic compounds, magnetite content must be extremely low. Certainly there are ferrimagnetic constituents in these rocks, but experiments using χ methods, such as thermomagnetic susceptibility measurement, as opposed to RM measurement techniques, best characterize the relative contributions of mineral constituents to χ. When such measurements are performed, χ has been shown to commonly be dominated by paramagnetic components, with a small ferrimagnetic component that is usually present but often does not dominate the χ (i.e., Ellwood et al., 2008). In almost all of these measurements, however, the detrital/eolian components that include both paramagnetic and ferrimagnetic constituents, are controlling the χ signal.

2.3. The effect of carbonate percentage on χ in marine sediments

In many instances, the χ in marine sediments has been shown to be *inversely* proportional to the carbonate content. This has led some workers to the false perception that χ variations in marine sediments are due to changing calcite concentrations, rather than to changes in the detrital/eolian component. It is clear that as the calcite volume

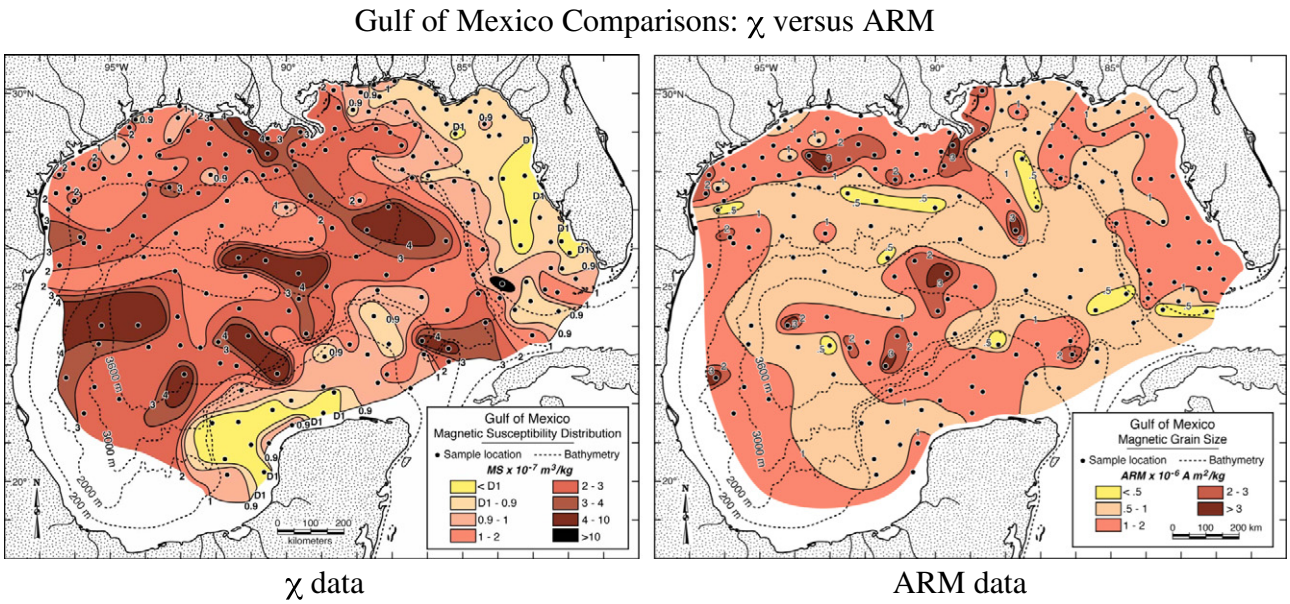

Fig. 2. χ and ARM variations for >200 core top and grab samples from the Gulf of Mexico illustrating the asymmetry between χ and RM methods. Modified from Ellwood et al., 2006.

in a sample increases, the detrital/eolian component responsible for the χ decreases, because the two concentrations are inversely related. These results are often misinterpreted, in part due to the way carbonate/detrital/eolian percentages are usually determined for sedimentary samples. The carbonate proportion of sediments is easily measured by acid digestion of the carbonate, and other methods, with the non-carbonate residue, detrital/eolian and non-carbonate marine, usually siliceous part of the sample, containing the minerals responsible for χ. Because such measurements focus on the carbonate percentage, some have taken the results to indicate that the carbonate content, perhaps driven by productivity, is responsible for changes observed for χ. Why is this conclusion false? It is important to remember that correlation is not causation. Consider a simple experiment with a pure carbonate sample to which a very small amount of paramagnetic or ferrimagnetic material is added as a 'contaminant'. Ellwood et al. (2000) conducted such experiments by incrementally adding powdered tourmaline, and other paramagnetic and ferrimagnetic compounds, to a pure calcium carbonate sample. They showed a linear, perceptible increase in χ as more and more tourmaline was added. In these experiments, Ellwood et al. (2000) used tourmaline percentages of ~1, 2, 9 and 16.5%, resulting in an inverse correlation between the carbonate content and the χ. The factor controlling χ in such cases is the contaminant compound, such as the tourmaline used in one of these experiments, biotite in another, and other contaminants, that act as the detrital/eolian component.

When it is considered that the χ of diamagnetic compounds, such as calcite or quartz, is negative and many orders of magnitude lower than χ for any paramagnetic or ferrimagnetic detrital/eolian constituent, it is mathematically and experimentally evident that χ measured for marine samples does not result, in any significant way, from productivity or the influx of either calcite or quartz. Rather, experiments have shown that the addition of calcite at normal marine productivity levels has very little effect on the measured χ (Ellwood et al., 2000; Febo, 2007; Febo et al., 2007). Only when large amounts of calcite are added to the system, is there a significant change in the χ. For example, consider another simple experiment. If 50% of calcite was added to a sample, and the detrital/eolian component was held constant, χ will fall, but by only a very small amount due to the dilution effect of the calcite. However, if only 1% of a paramagnetic component is then added to the same sample, χ will show a significant increase, much greater than the relatively small decrease produced by adding much larger quantities of calcite. It is not the change in the quantity of calcite, but rather the change in the paramagnetic or ferrimagnetic component that exerts the dominant control on χ in these samples. To underline this point, it was shown in some experiments that it takes >800% calcite dilution to drop χ by just one order of magnitude (Febo, 2007; Febo et al., 2007).

Ultimately, following diagenesis, χ observed for most marine sedimentary rocks can be used as a proxy for physical processes responsible for delivering the detrital/eolian component of these sediments into marine sedimentary basins. These processes are both regional and global and include climate, volcanism, tectonic processes, relative sea-level changes and eustacy.

2.4. Field gamma radiation spectroscopy (GRS) and ^{40}K laboratory measurements

GRS field instruments are reasonably sensitive, but the area of sample measured is larger than close-interval sampling can resolve, so that field measurements tend to result in a smoothing effect throughout a stratigraphic sequence. This enhances large-magnitude GRS anomalies but such measurements tend to lose the fine-scale cyclicity. Laboratory measurements, allow for isolation of high-resolution, close-interval samples and produce data sets from which cycles can be extracted. In the measurements reported here, ^{40}K gamma emissions are used because it is an isolated peak not associated with energies from other near-by radionuclides to affect it, and due to uncertainties in daughter product emissions associated with U or Th decay series, the lower mobility of ^{40}K as a stratigraphic component, and the abundance of potassium in detrital/eolian minerals deposited in the marine system. Because ^{40}K is known to exist in a fixed ratio relative to stable and abundant ^{39}K and ^{41}K, and ^{40}K only makes up 0.012% of all naturally occurring potassium and has a geologically long half-life, simple chemical measurement of bulk potassium should provide a proxy for ^{40}K, when ^{40}K is difficult or impossible to measure. In turn, ^{40}K should provide a proxy for total K in a sample. However, if the chemical measurement technique, for example ICP versus XRF, or other methods and sample preparation techniques do not identify all the K in a sample, then a correlation error is introduced.

There are trade-offs when measuring ^{40}K using laboratory measurements that must be recognized when reporting such measurements. Because samples are relatively small, ^{40}K concentrations are quite low and therefore counting time must be increased to accommodate such small sample sizes. This creates uncertainties in measurement. A test of changing counting time and varying sample sizes is discussed below.

2.5. Magnetic (Fe) and ^{40}K mineralogy

There are many detrital/eolian compounds in marine sediments that contribute to the χ and gamma radiation. The most abundant of these includes a suite of K- and Fe-containing paramagnetic compounds dominated by phyllosilicates. In addition, there are other paramagnetic ferromagnesian minerals, iron sulfides, iron oxyhyroxides and iron carbonates that are often significant contributors to χ. Also, ferrimagnetic minerals, mainly magnetite, are present, although other ferrimagnetic iron oxides, sulfides and sulfates, are also often present. Potassium-bearing minerals that are very abundant, in addition to phyllosilicates, are K-feldspars. Clays are also often abundant in marine sediments, and these minerals can be the main contributor to the measured χ, and often to the ^{40}K radiation.

Two of the most important phyllosilicate minerals in marine sediments for χ and GRS analysis are illite and chlorite. Both often contain abundant iron, but, whereas illite also has abundant potassium, chlorite does not. Therefore, both illite and chlorite should exhibit a strong paramagnetic χ signal, whereas illite, with high potassium concentrations, will also produce high ^{40}K counts; but chlorite will not. Biotite, while not as abundant as illite and perhaps chlorite, is often found in lithified marine sediments (Ellwood et al., 2000), and has high K and Fe. Therefore, biotite should contribute significantly to the χ and ^{40}K radiation when present. On the other hand, muscovite is generally low in Fe but high in K, so it will mainly contribute to the ^{40}K radiation in a sample. K-feldspars have high concentrations of K but usually very little Fe, again resulting in high ^{40}K but low χ values. Given that most of these minerals are primary constituents of the detrital/eolian component dispersed into the marine environment, they should provide an interesting contrast between the gamma radiation and χ signatures. In addition, smectite (montmorillonite) and kaolinite both are usually low in K and Fe, and thus when these clays are abundant, unless contaminated, they would be expected to reduce the overall χ and ^{40}K signals as a result of dilution of the more paramagnetic and K-containing components present.

2.6. Event and cyclostratigraphic variations

Event and cyclostratigraphic variations characterize the two main effects producing the detrital/eolian signal observed in marine sedimentary rocks; (1) climate cyclostratigraphy represented by relatively uniform, high-frequency climate-controlled erosional events, and (2) event stratigraphy due to global, short-term eustatic perturbations such as caused by impacts (Ellwood et al., 2003). It is during these eustatic events that the high values produced in GRS, the ^{40}K, and by proxy total K, and χ are observed. When taken together, these parameters can be traced globally. Event and cyclostratigraphic results are represented in most χ and gamma radiation data sets, as (1) weak to moderate cyclic and non-cyclic pulses, and (2) strong erosional pulses. Both are responsible for bringing detrital/eolian components into the marine environment, but they are represented in χ and gamma radiation data sets differently. During weak to moderate climate cycles, where erosional rates are relatively low, the correspondence between χ and gamma radiation peaks, represented by differing detrital/eolian mineral components, tends to show lower correlations than when there are significant, large-magnitude but short-term event-driven erosional pulses. The accumulation in marine sediments of large-scale, pulse-driven, event, detrital/eolian components results in a sequence of ^{40}K, total K and χ peaks that are well correlated due to the abundant and relatively consistent input of a wide range of paramagnetic and K-bearing constituents during these times. These pulses produce the occasional, large event peaks with correlated χ, GRS and K highs that are found in stratigraphic sequences. Such events are due to large-scale tectonic, volcanic or other processes that either affect eustacy and significant base-level change, or produce abrupt, non-cyclic eolian pulses.

3. Methods

3.1. Field sampling

In the field the section being sampled was cleaned using scrapers and brushes, so that all beds and lithologies were well exposed. Highly weathered zones were cleaned by digging, chipping and brushing. Approximately 30 g samples were collected at ~5 cm intervals for χ, gamma ray and geochemical measurement, and returned to the laboratory for study. Such close interval sampling techniques provide a robust data set that allows confidence in single measurements. Field measurement of χ and GRS is quite useful because they are fast and much less time intensive than are laboratory-based measurements. However there is concern that there is increased scatter in such measurements, due to inherent problems such as surface contamination, detector position, and for GRS, sample counting time and the cone of acquisition of gamma radiation that is much larger than an individual sample-size represents.

3.2. Laboratory and field measurement of magnetic susceptibility (χ)

Laboratory χ measurements reported in this paper were performed using the susceptibility bridge at LSU, calibrated relative to mass using standard salts reported by Swartzendruber (1992) and CRC Tables. χ is reported here in terms of sample mass because it is much easier and faster to measure with high precision than is volume, and it is now the standard for χ measurement. The low-field χ bridge at LSU can measure diamagnetic samples at least as low as -4×10^{-9}. This is illustrated by two relatively pure calcite samples collected from a core drilled from a standing, isolated speleothem in Carlsbad Caverns National Park (Brook et al., 2006), with measured values and standard deviation for three replicate measurements for each sample of -3.37×10^{-9} +/− 7.64×10^{-11} and -3.46×10^{-9} +/− 8.69×10^{-11} m^3/kg, respectively.

Field measurements were made on Devonian limestone, marl and shale lithologies from Morocco using a Bartington MS2 Magnetic Susceptibility Meter with a ~15 mm coil positioned at the end of a probe as the sensor. The instrument is first zeroed with the probe held away from the outcrop, then placed against the outcrop at the point of measurement, and the susceptibility measurement is then taken. The instrument produces a number representing initial counts and this can be used in calculating the susceptibility value, or simply used as a count value representing general changes in susceptibility magnitude. Field measurements were made at a measured point in the section before the laboratory samples were collected at the same point. A comparison for 1563 samples measured in the field with those measured in the laboratory is given in Fig. 3. Comparison between field counts and laboratory χ data demonstrates that there is a reasonable correlation between the two methods used, with an $r^2 = 0.736$ for 1563 data points (Fig. 3). However, there is also considerable scatter. Not surprisingly, much of the scatter is at higher χ values. The fact that χ values for marine rocks mainly fall in the range from 1×10^{-9} to 2×10^{-7}, and that the median value is around 5.5×10^{-8}, results in the visual scatter apparently being lower because χ values are clustered toward the origin in Fig. 3, where the field instrument is unable to resolve counts with any precision.

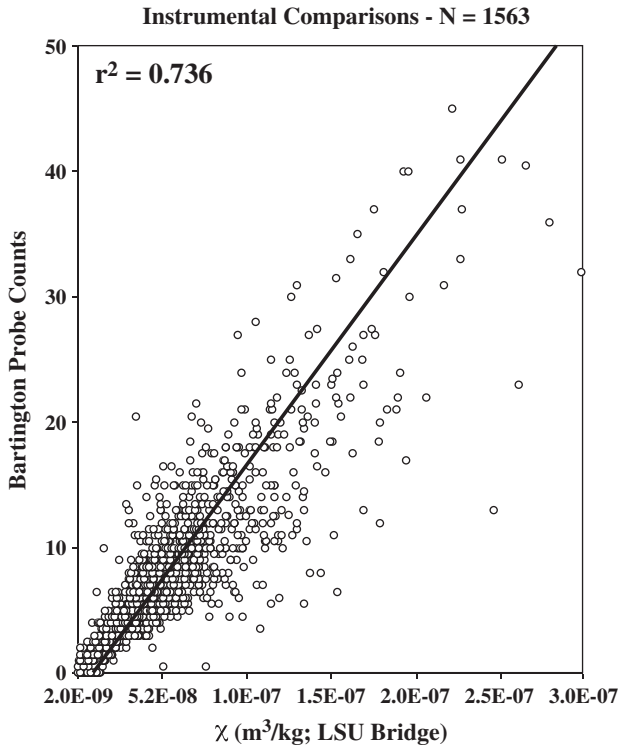

Fig. 3. Comparison for 1563 magnetic susceptibility measurements using field and laboratory equipment. Samples were measured and collected for multiple geological sections in the Anti-Atlas region of Morocco.

3.3. Laboratory and field measurement of gamma radiation

Samples, collected at 5 cm intervals from each C–T section, were cleaned, crushed and placed in a plastic Petri dish (0.05 m in diameter) for gamma ray measurement. The mass of the sample was measured and the sample was then placed on a Canberra high-purity germanium (HPGe) gamma spectroscopy detection system with 4096 nominal energy channels (up to 2 MeV) to determine the activity of ^{40}K, ^{232}Th, and ^{238}U in the sample. Each sample was measured for 1 h. Radioactivity of ^{40}K was measured directly with energies of 1460.8 +/− 5 keV. Radioactivity of ^{232}Th and ^{238}U was estimated from its decayed progenies, ^{212}Pb for ^{232}Th at energies of 238.6 +/− 5 keV, and ^{214}Bi for ^{238}U at energies of 609.3 +/− 5 keV. These decayed progenies have relatively high radiation yields for the desirable photon energy emissions and detection efficiency for the HPGe detection system, and are optimum for the small sample sizes, 10 to 30 g used. Also, ^{222}Rn loss from samples of naturally occurring radioactive material is usually less than 5%. ^{40}K results are reported in counting rates (counts per hour) per gram. U and Th proxies are not reported here.

An experiment to evaluate the reproducibility of laboratory counting times and sample size was conducted on a carbonate-rich sample from a C–T boundary interval section in England. The sample was split into ~2, ~5, ~10 and ~15 g sizes and then each of these splits was measured for 5, 40, 60, 120 and 300 min, and the ^{40}K data reported in two ways (Fig. 4a and b). Fig. 4a illustrates the scatter for each time and mass used and shows that when sample size approaches 10 g with a measurement time of 40 min or greater, the reproducibility is high. After evaluating Fig. 4a, it was decided to use 60 min as the standard counting time. Measurement mass was then varied from 2, 5, 10 and 15 g, and results then evaluated in Fig. 4b. The result of counting each sample mass six different times for 60 min each, illustrates that the scatter is low for samples approaching 10 g, with a mean value of 0.98 +/− 0.35 counts/h/g. The 15 g sample exhibits a mean value of 1.07 +/− 0.27 counts/h/g. Given the standard deviations for these two sample sizes, the end result is that the means are indistinguishable between samples with a mass of 5, 10 or 15 g, although the scatter is clearly higher in the 5 g sample (Fig. 4b). While outliers appear to be generally lower than the mean, the precision of measurement on such a weak sample is quite good. Based on these results, measurements reported here were made for 60 min, with sample masses, if possible, of 10 g or greater.

When measuring GRS in the field, a Radiation Solutions RS 230 BGO Super-SPEC handheld gamma-ray spectrometer was used. In this work, measurement interval was 5 cm and measurement time was 120 s. The RS 230 is calibrated to yield results for ^{40}K directly at energies from 1370 to 1570 keV, ^{214}Bi as a progeny for ^{238}U at energies from 1660 to 1860 keV, and ^{208}Tl as a progeny for ^{232}Th at energies from 2410 to 2810 keV.

3.4. Elemental determinations using XRF

Element concentrations were determined using pressed pellet preparation on a Bruker S4 wavelength dispersive X-ray fluorescence (WD-XRF) instrument. Preparation and analytical methods resulted in determination of 10 major elements, Al_2O_3, SiO_2, TiO_2, Fe_2O_3, MnO, MgO, CaO, K_2O, Na_2O and P_2O_5, reported at weight percentage oxides and 25 trace elements, S, Cl, As, Ba, Co, Cr, Cs, Cu, Ga, Hf, La, Mo, Nb, Ni, Pb, Rb, Sc, Sr, Ta, Th, U, V, Y, Zn and Zr, reported as ppm. Accuracy and precision were monitored using in-house rock standards, which were run every 10th sample. Additionally selected samples were run in triplicate during each batch.

Variations in elemental concentrations determined by XRF (or ICP) are commonly used to define chemostratigraphic correlations. Most commonly, chemostratigraphy has been applied to provide correlations between relatively closely spaced sections for the petroleum industry (e.g., Pearce et al., 1999; Ratcliffe et al., 2004, 2010). The resultant chemostratigraphic correlations are based upon changes in chemistry that reflect subtle changes in mineralogy, which in turn reflect changes in sediment provenance (Ratcliffe et al., 2004, 2008; Wright et al., 2010), changes in facies (Svendsen et al., 2007), or changes in paleoclimate (Pearce et al., 2005; Ratcliffe et al., 2010). By enabling very subtle changes in such parameters to be modeled, the technique is capable of providing high resolution correlations. Typically, such correlation schemes are essentially lithostratigraphic and therefore any stratigraphic correlation is likely to be of restricted extent. However, it has been demonstrated that chemostratigraphic interpretation enables chronostratigraphic events to be correlated globally by recognition of T–R cycles (Ellwood et al., 2008). For the purposes of this paper, just K, determined by XRF analysis, was used to compare to the ^{40}K data sets. Much of this chemostratigraphic work is included in a paper currently in review.

3.5. Presentation of χ data

Because χ and gamma radiation data sets are cyclic, for the purpose of correlating among geologic sequences and graphic comparison with climate models, a bar-log plotting convention is used, such that if a cyclic trend is represented by two or more data points, then this trend is assumed to be significant and the highs and lows associated with these cycles are differentiated by black (i.e., high χ values) or white (i.e., low χ values) bar-logs. This method is best employed when high-resolution data sets are being analyzed (large numbers of closely spaced samples). High-resolution data sets help resolve χ and gamma radiation variations associated with anomalous samples. Such variations may be due to (1) weathering effects, (2) secondary alteration, (3) metamorphism, (4) eustacy, (5) short term climate variations, and to other factors. In addition, variations in detrital/eolian input, or a change in detrital/eolian sediment source is resolved by developing and comparing bar-logs between different localities.

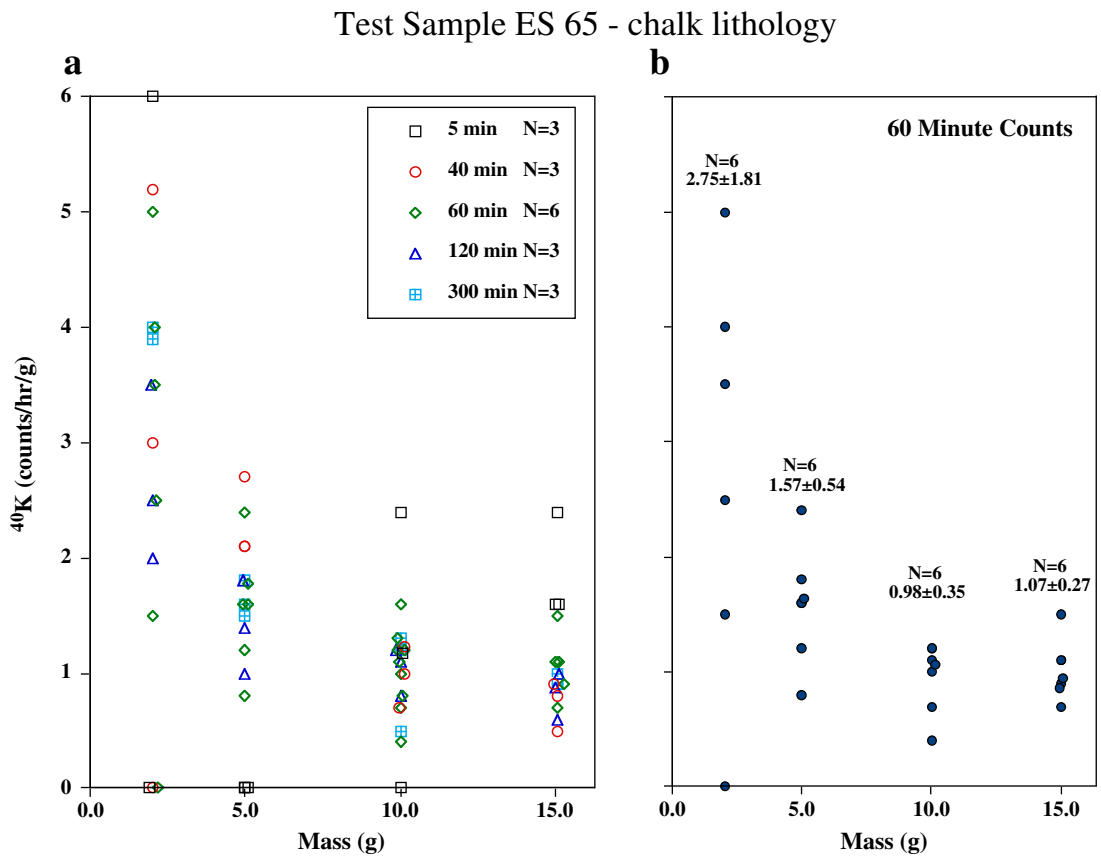

Fig. 4. Experimental evaluation of the reproducibility for laboratory ^{40}K gamma radiation measurements using a test sample (ES 65) from the C–T Eastbourne chalk section in England. (a) Replicate measurement of ^{40}K for ES 65 for different counting times and different masses. (b) Replicate measurement of ^{40}K for ES 65 for different masses using only a 60 minute counting time.

4. Results

4.1. χ comparison: C–T GSSP to the S Section

A χ data set for part of the GSSP was previously published (Ellwood et al., 2008). This section is extended here to >12 m by sampling ~4 m down into the Hartland Shale and constructing a composite section for this locality (Fig. 5). In addition, a second C–T boundary section, the S Section, was collected from ~1 km to the SW of the GSSP railroad cut (Fig. 1). This coeval section was sampled previously for biostratigraphic analysis by Keller et al. (2004). Lithostratigraphic comparison between the GSSP and S Section lithogies indicate fairly good agreement with some slight differences in bed position and thickness, as would be expected. In addition, weathering in the S Section appears to have altered Bed 77 into two thin limestone lenses, and has enhanced the appearance of thin bentonite Bed 82 above Bed 80. While both sections were exposed at about the same time that the Lake Pueblo dam was built (Fig. 1), the steeper railroad cut GSSP section appears to be somewhat less weathered than is the S Section. This is due to faster erosion in the GSSP section, thus limiting time for weathering. χ data comparisons in Fig. 5 show similar variability and trends between the two sections.

4.2. GRS field measurement comparison: C–T GSSP to the S Section

Field measurements using the Radiations Solutions RS 230 GRS instrument were made at 5 cm intervals from within the top of the Hartland Shale just below Bed 63 to the boundary at the base of Bed 86, and then up to the top of Bed 86 in both the GSSP and S Sections. The purpose of making 5 cm interval measurements was to test usage of a field instrument of this type to determine if high-resolution results could be acquired. While there is a generally good correlation between the two sections for ^{40}K, Th and U counts, the large sensing cone of the instrument results in a broadly smoothed-looking data set (Fig. 6). In the lower one-third part of the two sections, the agreement is not as good as in the upper two-thirds, due to differential weathering between the two sites. It appears that the enhanced GRS values, associated with bentonites in both sections, are muted and broken up in the S Section.

Field GRS measurements are compared to laboratory ^{40}K and χ data sets among the two sections in Fig. 7. Laboratory measurements clearly produce higher resolution results than do field measurements, and comparative differences between sections are striking. For example, in the S Section, there are some close similarities in GRS and ^{40}K peak locations (Fig. 7e and f) that generally reflect the major trends observed in Fig. 6. However, in detail this breaks down somewhat in the lower part of the section, where weathering appears to be greatest. Laboratory χ and ^{40}K measurements for both the GSSP and S Sections show fairly good correlations, with generally matching within-section peaks (Fig. 7a and b; d and e). However, comparison among laboratory and field measurements for GRS values in the GSSP section show large differences that are not well correlated (Fig. 7b and c). In addition, ^{40}K laboratory data-set comparisons among the two sections are very different (Fig. 7b and e).

4.3. Geochemical and geophysical comparisons

GSSP and S Section measurements were compared by plotting χ versus elemental K, and ^{40}K measured in the laboratory (Fig. 8), and

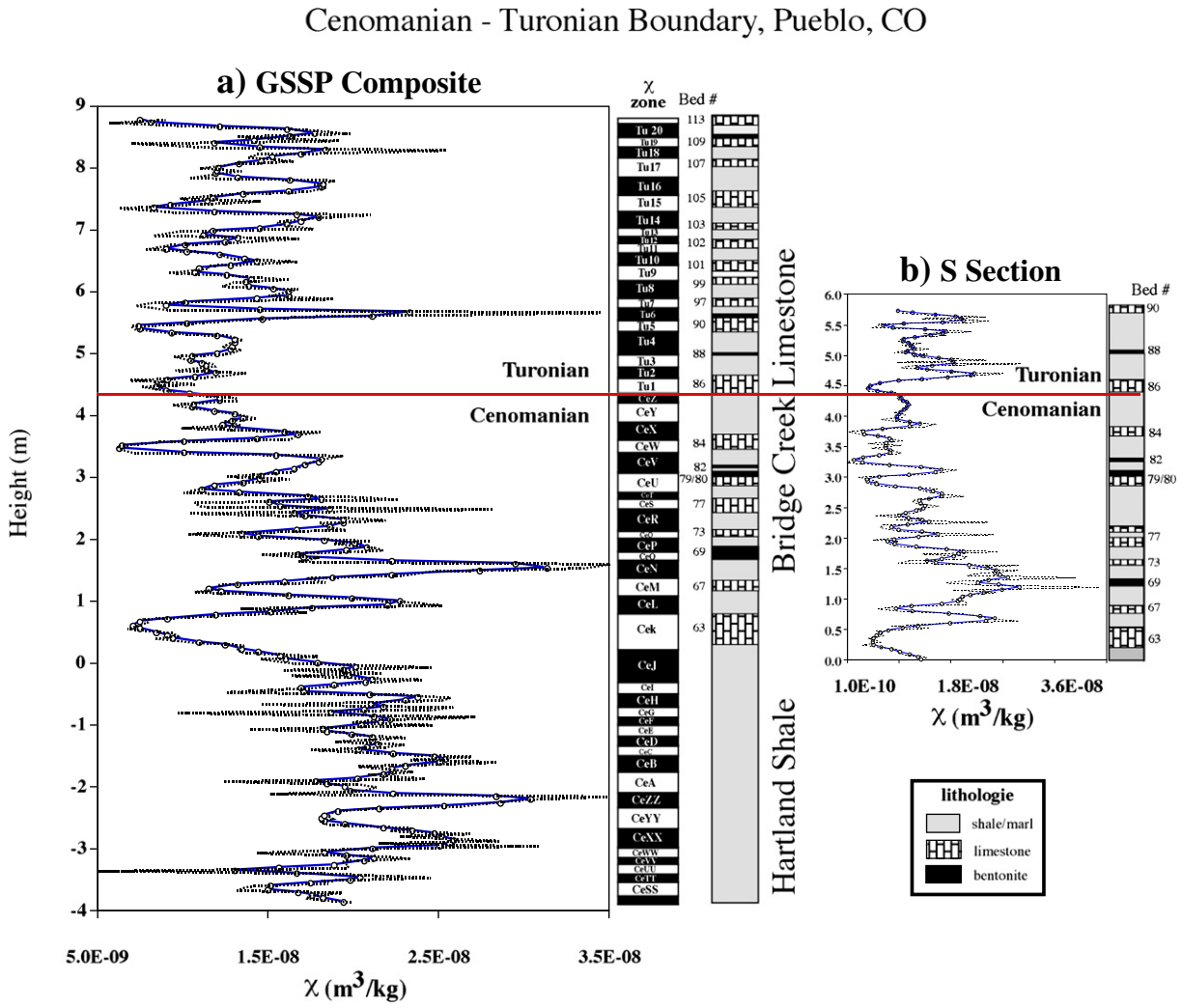

Fig. 5. χ data and lithologies for the (a) C–T GSSP and (b) S Section. Dotted curves are raw χ data in m^3/kg; solid curves are smoothed fits using splines. χ and model zones are labeled using the nomenclature from Ellwood et al. (2008). Bar-log is constructed from the raw data and represents highs and lows in the χ cyclicity for the GSSP section. Bed numbers and lithologies (shale [dotted], limestone [bricks], and bentonite [filled]; see lithology box) are given. The GSSP section represents a composite of the Hartland Shale and Bridge Creek Limestone members of the Greenhorn Formation and is an extension of the earlier work of Ellwood et al. (2008).

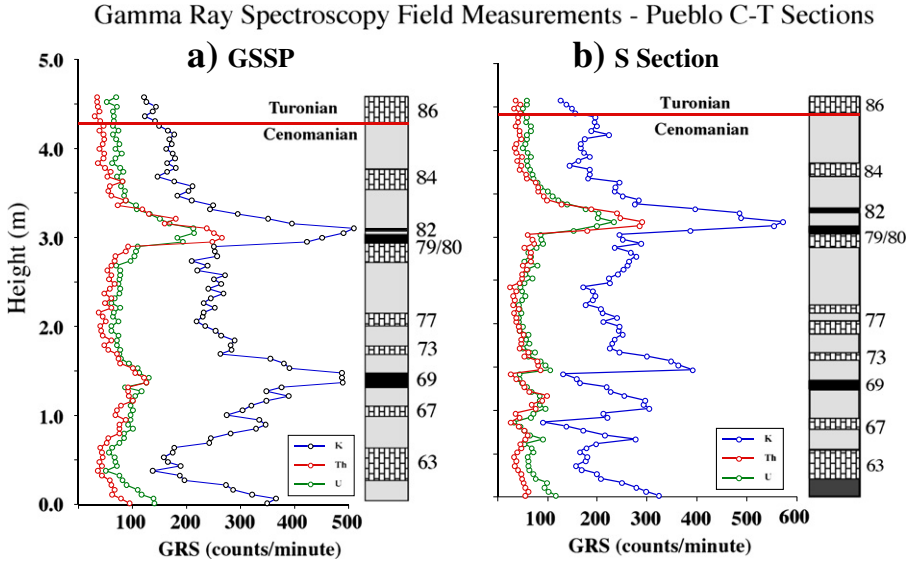

Fig. 6. GRS field measurements for the (a) C–T GSSP and (b) S Section. Curves are given for ^{40}K, Th and U in counts/min. Lithologies and bed numbers as in Fig. 5. This section comparison was performed only from the top of the Hartland shale (ending at the base of Bed 63) through the top of the GSSP boundary bed (Bed 86). High ^{40}K values relative to Th and U are an artifact of field instrument detectors, and not the result of high relative percentages among these elements.

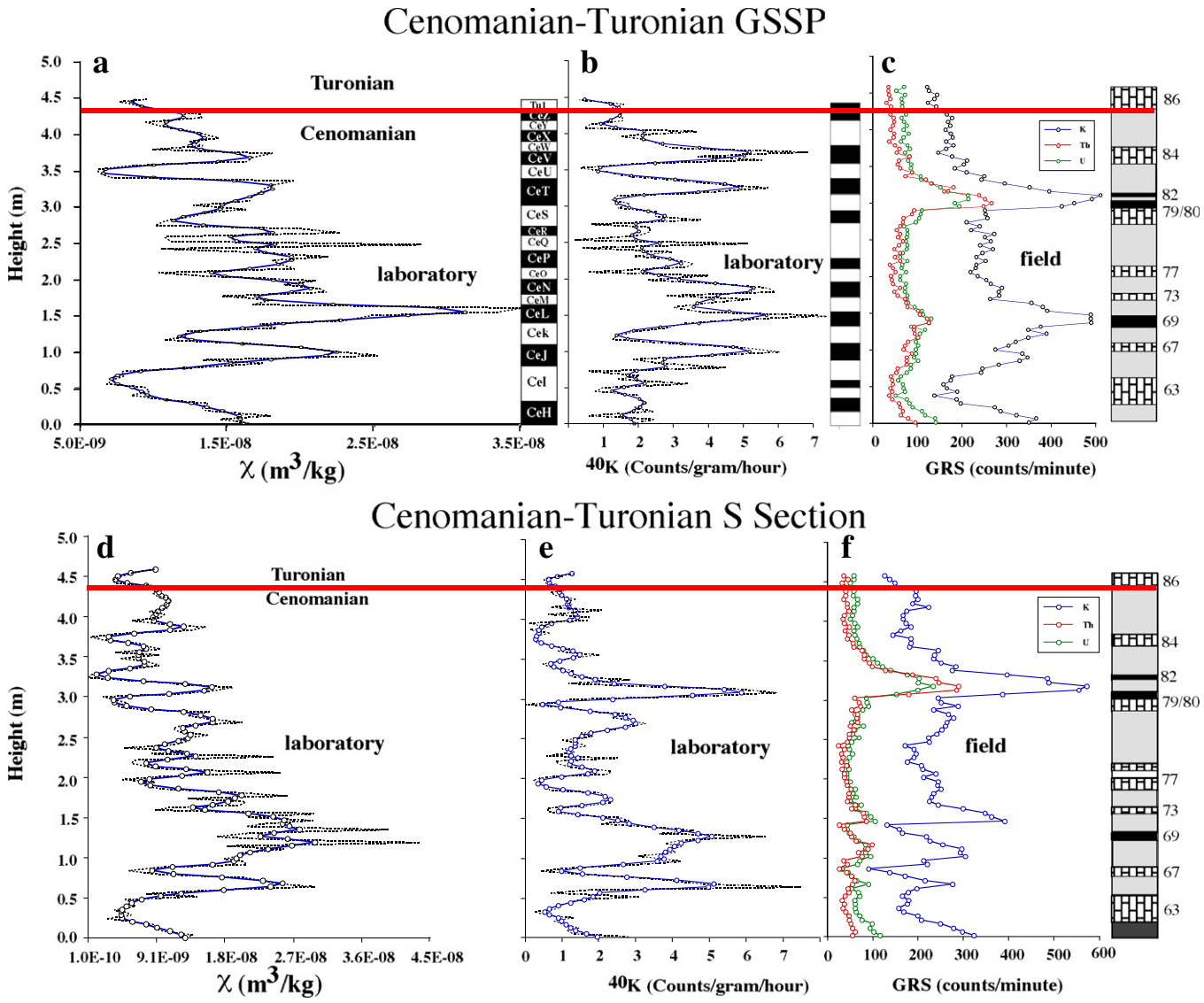

Fig. 7. Comparison of the χ laboratory (a, d), ^{40}K laboratory (b, e), and GRS field (c, f) measurements within and between the GSSP (above) and the S Section (below). χ and ^{40}K data are represented by dotted (raw data) and solid (smoothed data using splines) curves. Lithologies, nomenclature and bed numbers as in Fig. 5.

^{40}K measured in the field. The statistics for these comparisons are given in Table 1, as well as a comparison between K measured using XRF and ^{40}K measured on the same samples. Because the detrital/eolian constituents are the dominant sources for χ and elemental signatures in marine sediments, a strong positive correlation was expected for these comparisons. This was confirmed by the laboratory measurements on individual samples. This suggests that χ, K and ^{40}K can be used, with some reservations, as proxies for each other. However, comparison between laboratory and field measurements is generally significantly less well correlated (Table 1). While there is a reasonable correlation among these parameters for GSSP samples, and excellent in the case of χ and GRS field measurements, there is no correlation for S Section samples among field and laboratory measurements. This lack of correlation is interpreted to result from weathering and partial removal of elemental constituents from the S Section.

In order to examine each section in detail, and to make direct comparison between the χ and ^{40}K, laboratory derived data sets from Fig. 7 (Fig. a,b and d,e), the raw data from the GSSP and S Sections have been normalized and then smoothed using splines to hold stratigraphic position (Fig. 9). The result of these comparisons within each section is very good for major peaks (# in Fig. 9), but somewhat less well defined for lower magnitude trends (* in Fig. 9). This effect appears to be somewhat muted in the more weathered S Section. Note that each section is slightly different in terms of bed location within these sections, resulting in slight peak offsets between the GSSP and S Sections. This is evident from the lithologic logs given in Figs. 5–7. In these sequences, the highest χ and GRS values are found associated with bentonite Beds 69 and 80–82, and in some of the shale samples.

To further test the correlations between the χ and ^{40}K data sets, a segment of the χ bar-log has been constructed for the GSSP and compared to a ^{40}K bar-log built from the cyclic GSSP ^{40}K data set (Fig. 10). The dashed line represents a line-of-correlation fit through the tops and bottoms of corresponding bar-log segments. Accounting for the slight offsets in lithology and the very different origin of the χ and ^{40}K signals, the agreement is quite good. However, there are two anomalous half cycles observed in Fig. 10, one associated with Bed 63 in the ^{40}K data set and the other between Beds 84 and 86 in the χ data set. In the case of the χ anomalous half-cycle, there is a single higher ^{40}K value that corresponds to this χ half-cycle, but the rules for plotting bar-logs prohibit single data points from representing a half cycle. In the case of the ^{40}K anomalous half cycle, there is clearly

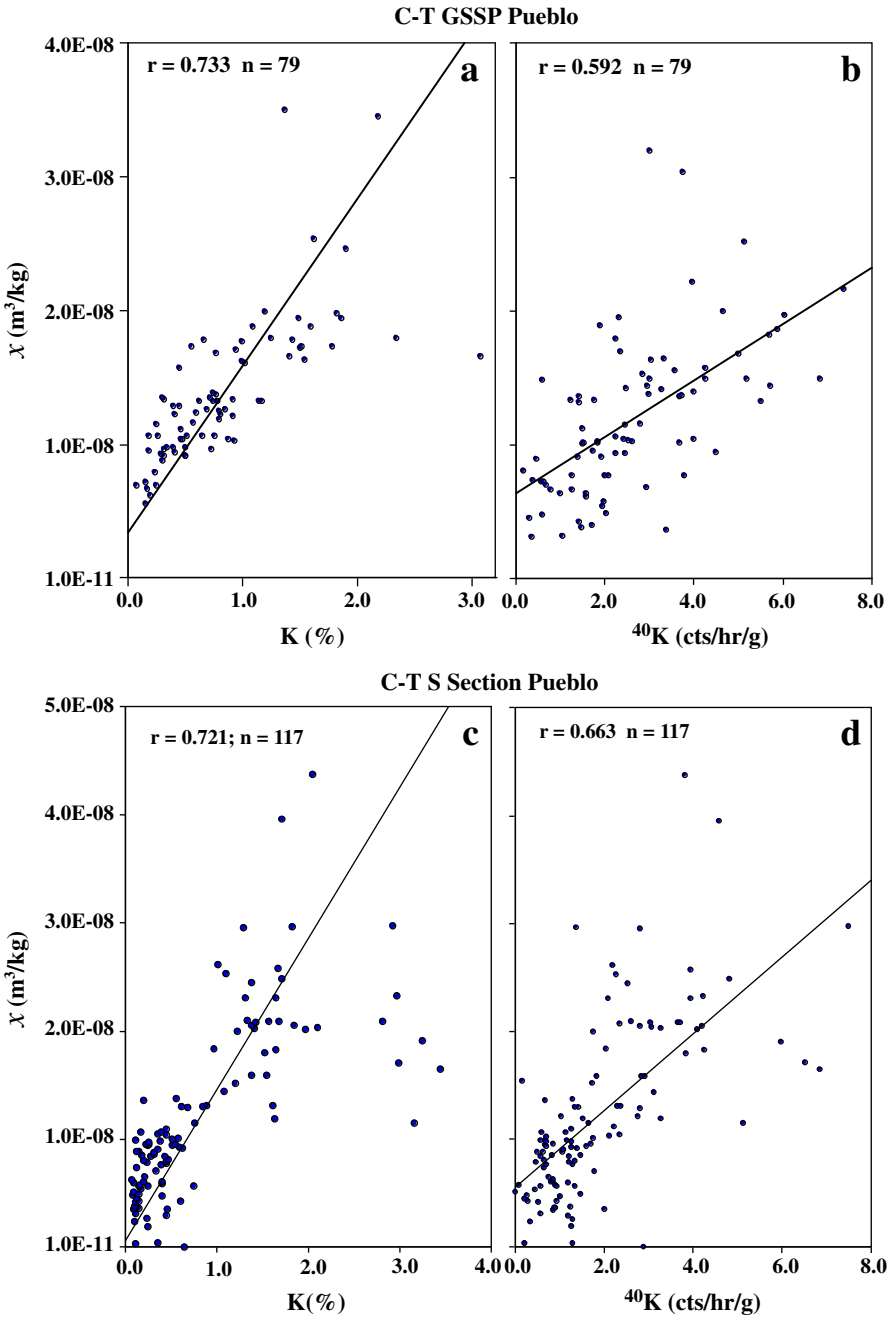

Fig. 8. Comparison of χ versus total elemental K, and χ versus ^{40}K measured in the laboratory for the GSSP (a, b), and for the S Section (c, d). K was only measured for every other sample in the GSSP; reported here from Bed 63 to Bed 86, the interval evaluated in this portion of the study. ^{40}K was measured on all samples available from the GSSP and the S Section through this interval.

at least one ^{40}K half cycle that is independent of the changes observed in the χ data set (*s in Fig. 9). These differences throughout the χ and ^{40}K data sets are due to the mineralogical differences discussed earlier in this paper.

4.4. Time-series analysis

Time-series analysis of the primary χ data independent of smoothing was performed for the sections sampled and results reported in Fig. 11a. To avoid introducing error, studied sections were selected where covered intervals could either be avoided or be sampled after careful cleaning of the section. Uniformly spaced samples were then collected and it was assumed that this uniform spacing is linear relative to time, i.e., Δx is proportional to Δt, so that harmonic analysis methods could be used. The less this assumption is true, due to variations in final sediment accumulation rate (SAR), differential diagenesis, or other factors, the more noise that will be produced in the spectral graph, and the less well defined will be spectral peaks (lower power).

The spectral power for the χ data sets was obtained using both the Multi-taper (MTM) and Fourier Transform (FT) methods after the data were both detrended and subjected to a Hanning window to reduce spectral leakage and increase the dynamic range (Jenkins and Watts, 1968; Thompson, 1982). Incidences of statistically significant peaks (at the 90, 95 and 99% levels) in the resulting spectra are determined by employing MTM (Ghil et al., 2002), as calculated with the SSA–MTM toolkit (Dettinger et al., 1995). A null hypothesis of red noise was assumed (low frequency high power in the spectrum,

Table 1
XRF, χ and GRS data for the GSSP composite and S Section. ^{40}K was measured in both the laboratory (Lab) and the field. All other results are from laboratory measurements on samples collected in the field. χ was only measured in the laboratory.

Parameters	C–T GSSP	% level	C–T S Section	% level
K Lab vs ^{40}K Lab (r)	0.522—n = 41	>99.9	0.916—n = 87	>99.9
K Lab vs ^{40}K Lab (r^2)	0.273—n = 41		0.839—n = 87	
K Lab vs χ (r)	0.687—n = 41	>99.9	0.721—n = 109	>99.9
K Lab vs χ (r^2)	0.473—n = 41		0.520—n = 109	
^{40}K Lab vs χ (r)	0.592—n = 83	>99.9	0.663—n = 92	>99.9
^{40}K Lab vs χ (r^2)	0.351—n = 83		0.439—n = 92	
^{40}K Field vs K (r)	0.514—n = 41	>99.9	0.055—n = 87	None
^{40}K Field vs K (r^2)	0.264—n = 41		0.003—n = 87	
^{40}K Field vs ^{40}K Lab (r)	0.381—n = 83	>99.9	0.050—n = 92	None
^{40}K Field vs ^{40}K Lab (r^2)	0.145—n = 83		0.002—n = 92	
^{40}K Field vs χ (r)	0.588—n = 88	>99.9	0.126—n = 92	None
^{40}K Field vs χ (r^2)	0.346—n = 88		0.016—n = 92	

sloping toward lower values at high frequencies), with a three taper model. As this method is prone to producing false positives, the use of statistical significance is limited here to its role in supporting (or not) the positions of multiple Milankovitch bands within the data set. The positions of these bands are fixed relative to each other, and so a climate forcing mechanism is supported by the spectral analysis when the Milankovitch frequencies are also frequencies of high spectral power. The MTM and FT methods, unlike the spline-smoothed χ data and bar-logs derived from these data sets, are capable of resolving high-frequency features in the data.

Based on the thickness for each section analyzed and the power in each FT peak, the locations of four to five major Milankovitch bands were calculated and placed in Fig. 11 at their relative position to each other within each data set. Because each section analyzed is a different length, the frequency is slightly different. The power spectrum for the GSSP χ data exhibits a region of above-average power, with eccentricity peaks, E2 at ~405 kyr and E1 at ~100 kyr showing good power. O2, and O1 obliquity peaks at ~50.5 and ~39 kyr, respectively, recalculated for the C–T boundary from Berger et al. (1992), assuming an age of ~93.9 Ma (Gradstein et al., 2012; Ogg et al., 2008), also show reasonable power (Fig. 11a). The power spectrum for the S Section χ data exhibits a region of above-average power, with eccentricity peaks, E2 at ~405 kyr, and E1 at ~100 kyr, while O2 and O1 are weak (Fig. 11b). The power spectrum for the GSSP GRS data set exhibits a region of very strong power for eccentricity peaks E2 and E1, with O1 exhibiting some power (Fig. 11c). The power spectrum for the S Section GRS data exhibits a region of above-average power for eccentricity E2 and E1 (Fig. 11d). These results are

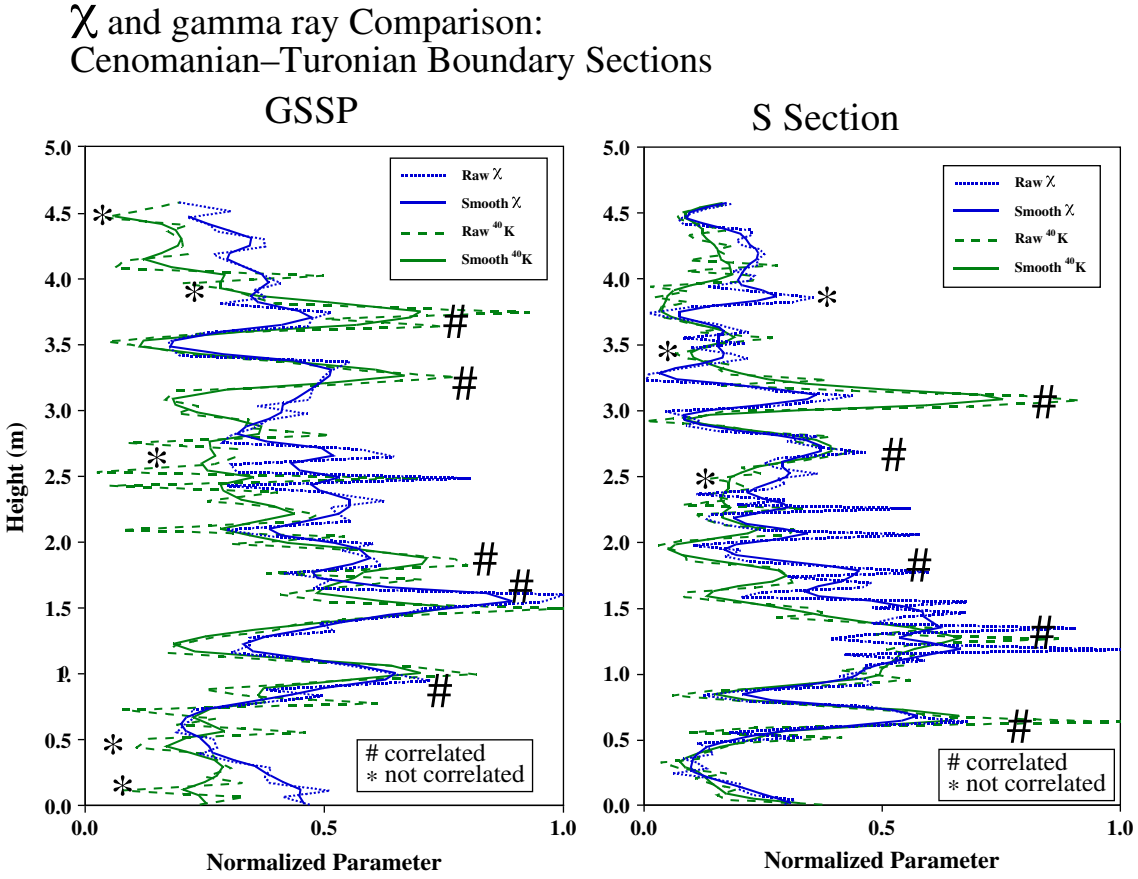

Fig. 9. Normalized plots of χ (raw, dashed blue; smoothed, solid blue) and GRS (raw, dashed green; smoothed, solid green) data comparison, measured in the laboratory, for samples from the GSSP and S Section; from the top of the Hartland Shale to the top of Bed 86 representing the C–T boundary. Initial data are given in Figs. 5 and 7. # = points where χ and ^{40}K peaks are well correlated; * = points where not correlated.

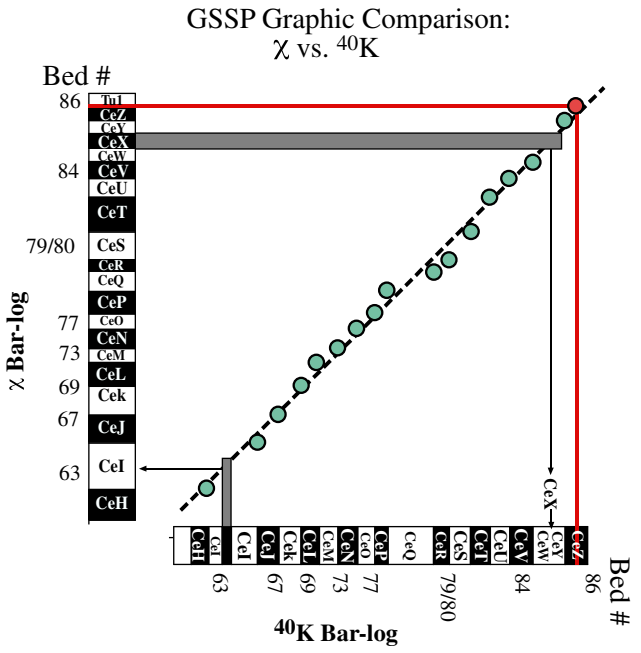

Fig. 10. Graphic comparison of χ and ^{40}K measured in the laboratory, using bar-logs constructed from measurements of samples collected from the C–T GSSP section. Circles represent juncture of tops and bases of bar-log half cycles. Dashed line is the line-of-correlation (LOC) fit through this data set. Shaded bars represent bar-log half cycles that are missing in the other data set and projected into the LOC. Red lines are placed at the base of Bed 86 and represents the C–T boundary location within this section. Bed numbers are from Fig. 5.

consistent with climate cyclicity and provide strong evidence in these sections for the E2 and E1 eccentricity Milankovitch bands, including the E1 peak at ~100 kyr, with good similarities for χ and ^{40}K data sets.

5. Discussion

5.1. Field versus laboratory χ and gamma radiation measurement evaluation

Comparison between χ field and laboratory measurements using the laboratory bridge at LSU and a Bartington field instrument showed generally the same trends (Fig. 3). However, due to the low sensitivity of such instruments and problems with probe placement in the field, it is argued that while the field instrument is good for quickly evaluating geological sections, field collecting and laboratory measurement is necessary for the high-resolution time-series and correlation work that are desired for many such studies.

When comparing field versus laboratory measurements for ^{40}K counts, it is clear that due to the large gamma ray acquisition cone, field GRS instruments are essentially smoothing out the climate variability, and therefore dominated by unique lithologies. In some instances, there is a very rapid and distinct change in GRS as lithologic boundaries are crossed during measurement, for example, the upper major peak in Fig. 6a and b. However, in general the peaks are relatively broad and in the case of the C–T boundary interval in Colorado, are dominantly reflecting the presence of gamma-ray-generating elemental constituents in the bentonites observed at the site.

To evaluate experimental precision for GRS and χ data sets, one way is to contrast multiple high-resolution data sets for sample-to-sample consistency. If these variations are very large and the curves are significantly saw-toothed in character, then the sample-to-sample consistency is poor. Another way is to compare coeval sections for field and laboratory measurements, as is reported here in Figs. 5–7. A third way is to measure replicates for each sample, and this is routinely done for all χ measurements reported here. However, replicates for all gamma radiation measurements are too time consuming, especially when each sample is measured for an hour, as in the case for the data acquisition process used here. Therefore, the replicate experiment illustrated in Fig. 4 was designed to evaluate, for very weak samples, how much mass and time is necessary for reasonable analytical precision. At optimum, for very low ^{40}K concentrations, ^{40}K gamma ray emissions of 1 count/h/g (Fig. 4), require at least 10 g of sample with a measurement time estimated to be at least 40 min. However, most samples are not that weak and will produce reproducible gamma-ray emissions for smaller samples with shorter measurement times.

5.2. χ comparison: GSSP to S Sections

Previous work has demonstrated a χ correlation of the GSSP with the USGS #1 Portland core, recovered ~40 km to the west of the GSSP section (Ellwood et al., 2008). An additional section, the S Section is added here. Even though it is somewhat weathered in the lower one-third, it also shows excellent correlation with the GSSP χ data set (Fig. 5). χ values for the GSSP section from Beds 63 to 90, equivalent in height and lithology to the S Section, exhibit a mean of 1.42×10^{-8} +/− 5.5×10^{-9}, while the S Section for the same interval exhibits a mean of 1.22×10^{-8} +/− 8.0×10^{-9}. Lower values and greater standard deviation in the S Section data set appear to result from weathering effects in the section, although the trends exhibited remain correlated. Both data sets show similar FT trends (Fig. 11), but the power in some lower frequency peaks is weaker in the S Section because of weathering differences, and fewer samples being available for analysis due to the fact that the section is truncated at its top.

5.3. A Floating Point Time Scale (FPTS) based on an E1 climate model

Because χ zones have been shown to represent Milankovitch climate cyclicity, it is possible to compare cyclic χ data sets to uniform climate models. This allows a χ data set to serve as a Floating Point Time Scale (FPTS). To develop a FPTS, FT time-series analyses were performed on raw (unsmoothed) χ data sets, and those Milankovitch bands representing strong power identified. Following FT analysis, the χ data were tuned to represent the approximate position of the E1 Milankovitch band that has strong power in most of the FT data sets given in Fig. 11, and χ bar-logs are constructed for comparison to the FPTS. These bar-logs, derived from χ zones, represent half cycles for the band or time selected, in this case the E1 obliquity at ~100 kyr, and a half cycle of ~50 kyr. An example of this type of analysis was presented by Ellwood et al. (2011) for the Givetian Stage in the Devonian. They chose the ~400 kyr band as the Milankovitch cycle that allowed them to establish a FPTS for the entire Givetian Stage in the Middle Devonian, with each half-cycle (filled or open χ bar-log segment) representing ~200 kyr. Once the zonation is established, depending on the absolute time scale and Milankovitch band used, it is possible to assign specific ages to each χ zone boundary and thus to estimate the timing of events recorded within a stratigraphic sequence. The χ bar-log zonation can then be compared directly to the FPTS uniform climate model to evaluate the SARs and rate variations within a succession.

In their paper, Ellwood et al. (2011) used GSSPs to anchor the ends of their composite section and to develop a χ standard reference zonation for the Givetian, and then tied their data set into a specific time scale using a published age for one of the GSSPs they used. In that case they demonstrated that the age for the Givetian from the time scale of Ogg et al. (2008) fit their data set better than did other time scales. They showed that this approach is useful for developing very high

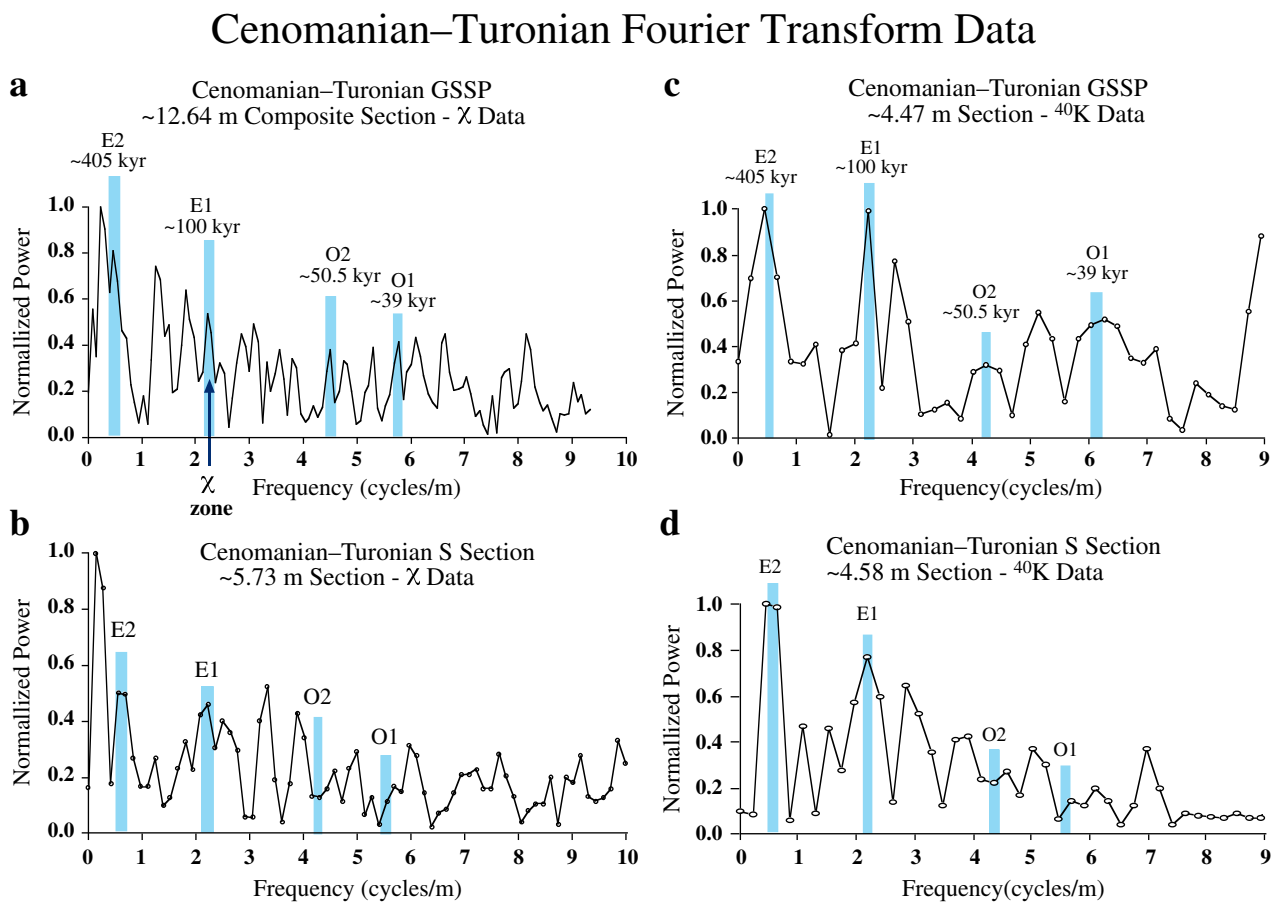

Fig. 11. Fourier transform (FT) frequency data (cycles/m) for the GSSP and S Sections presented in Fig. 3; (a) FT from raw χ data for the GSSP composite section; (b) FT from raw χ data for the S Section; (c) FT from ^{40}K lab based data for the GSSP portion of the Bridge Creek Limestone below the C–T boundary at Bed 86; (d) FT from ^{40}K lab based data for the S Section portion of the Bridge Creek Limestone below the C–T boundary at Bed 86. Position for Milankovitch bands are given for eccentricity (E2 ~400 kyr and E1 ~100 kyr), obliquity (O2 ~50.5 kyr and O1 ~39.0 kyr; calculated from Berger et al., 1992) and precessional (P2 ~22.3 kyr; calculated from Berger et al., 1992).

resolution ages that can be used in developing a good understanding of the timing of biostratigraphic and geologic events.

Using FT data from the C–T GSSP in Colorado, χ data from the GSSP have been smoothed using splines and tuned to closely approximate the E1 eccentricity band at ~100 kyr cyclicity. The χ smoothed curve used, and corresponding bar-log developed, are given in Fig. 5a. This zonation was initially established by Ellwood et al. (2008), and their labeling scheme has been applied to the new C–T composite section given in Fig. 5a. This is then graphically compared to a uniform FPTS model that represents ~100 kyr climate cyclicity, thus giving ~50 kyr resolution to the data interpretations (Fig. 12).

Two relatively long correlation trends in the graphic comparison in Fig. 12 are identified, and these are separated by a short jump in SAR at the transition from the Hartland Shale into the Bridge Creek Limestone. SAR in the lower Segment A is identified to be ~0.44 cm/kyr, in the transition zone it is much higher, at ~1.25 cm/kyr, but for a period of only ~100 kyr. In the longest data segment, B, the SAR is very similar to that in the Hartland Shale at ~0.47 cm/kyr (Fig. 12). Long-term cyclic variability is also observed superimposed on both long correlation segments. The variation represented by the long-term cycles visually evident within the Hartland Shale (Fig. 12) is interpreted to be the Milankovitch E2 eccentricity cyclicity (Fig. 11), argued to be expected in geological data sets (i.e., Shackleton et al., 1999; Laskar et al., 2004). Two similar long-term cycles are also represented within correlation envelope B (shaded Segment B in Fig. 12), observed for the Bridge Creek Limestone segment of the graphic comparison data set. This interval, extending through the C–T boundary, represents ~1.8 myr, with the time recorded in the entire composite section of ~2.7 myr. This result is slightly less than previously reported by Ellwood et al. (2008), and indicates better resolution for the extended GSSP section reported here.

Keller et al. (2004) evaluated SAR for the S Section, assigning ages to fossil first appearance (FAD) and last appearance (LAD) data, using published bentonites ages from the section. On average their results were essentially the same for the S Section as those reported here in Fig. 12 for the GSSP composite. While SARs are similar throughout the whole GSSP composite section, with the exception of the transition zone from the Hartland Shale into the Bridge Creek Limestone, their data for the S Section indicate two different SAR linear segments within the Bridge Creek Limestone, higher SAR at the base, with a shift at Bed 79/80 to a lower SAR at the top. It is argued here that these differences are due to large uncertainties in the radiometric data set used by Keller et al. (2004). In addition they identify a duration of ~650 kyr for deposition of that part of the Bridge Creek Limestone represented in the S Section. For the same interval in the GSSP, from slightly below Bed 63 to Bed 90 (Fig. 5a) a duration of ~1.05 myr is calculated here. Given the uncertainties, this agreement is excellent. Slightly higher numbers were reported by Sageman et al. (2006) for the same interval at ~700 kyr.

6. Conclusions

Low-field, mass-specific magnetic susceptibility (χ) and gamma radiation methods are measured in the field and on individual samples collected in outcrop to, evaluate field and laboratory measurements and to compare results from different stratigraphic sequences using

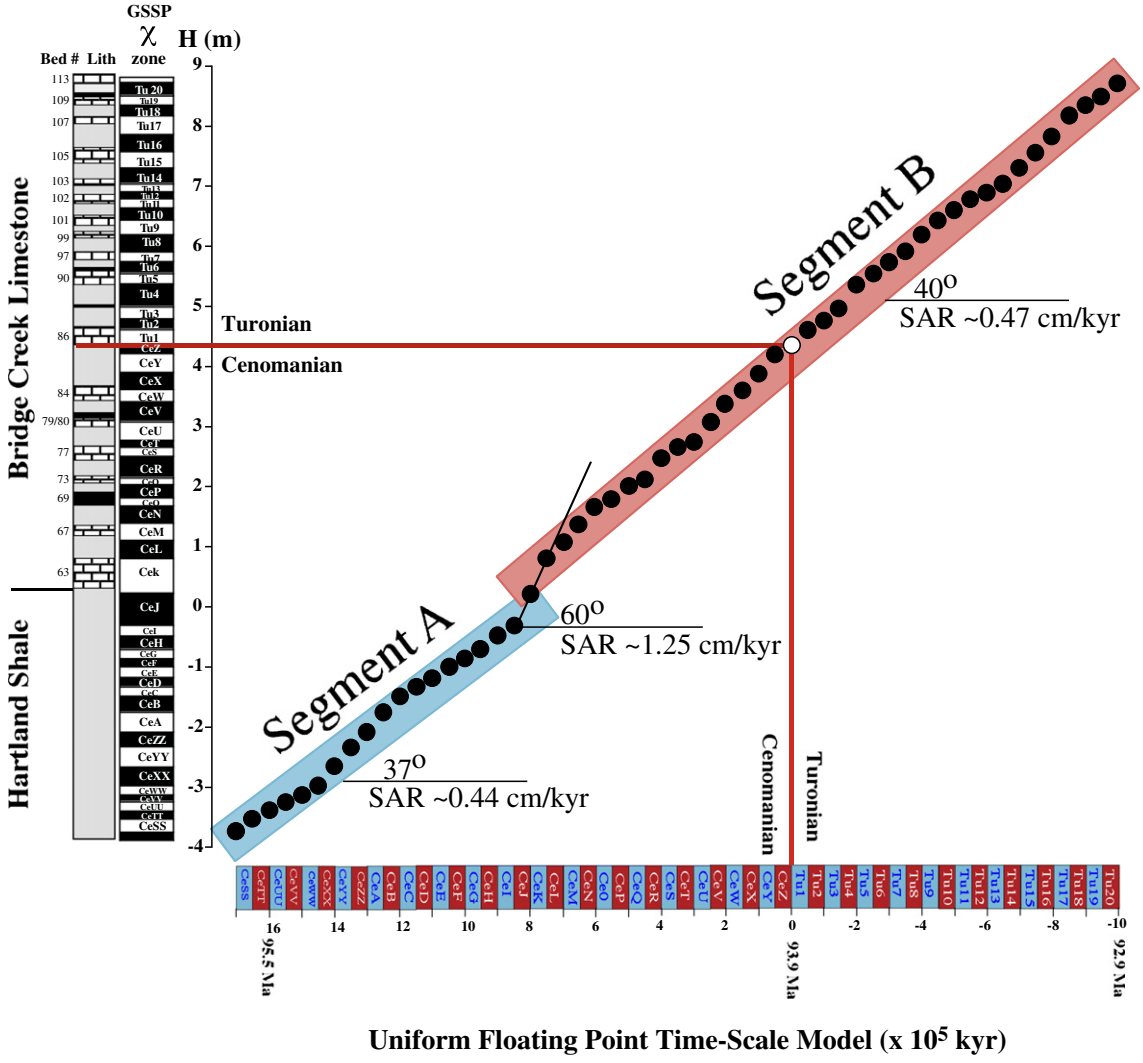

Fig. 12. Graphic comparison for the Pueblo GSSP composite with a uniform ~50 kyr floating-point time scale model. Black circles represent the intersection of corresponding χ zone tops and bases between the χ zones for the GSSP data developed for this study and the uniform time-scale model. Open circle represents the position of the stage boundary within the composite. χ and model zones are labeled using the nomenclature from Ellwood et al. (2008). Shading represents the mean line-of-correlation (LOC) for two sets of correlation data that exhibit a similar trend, with Segment A represented by the Hartland Shale part of the composite (at 37°), and exhibiting a final sediment accumulation rate (SAR) of ~0.44 cm/kyr. Segment B, represented by the Bridge Creek Limestone portion of the data set (at 40°), exhibiting a slightly higher SAR of ~0.47 cm/kyr. The transition from the Hartland to the Bridge Creek exhibits a short-term (at 60°) but high SAR of ~1.25 cm/kyr.

these two methods. The main work reported here is from two Cenomanian–Turonian (C–T) boundary sections from Pueblo, Colorado, within the Western Interior Seaway, the Global boundary Stratotype Section and Point (GSSP) and a nearby S Section. These experiments were designed to evaluate; (1) the combined potential of χ and field-based gamma-ray spectroscopy (GRS) as a correlation tool using well-studied C–T sequences, (2) the effect of weathering on χ and gamma radiation values, (3) the effect of changing lithologies on χ and gamma radiation values, and (4) the differences between field-based and laboratory-based measurements using χ and gamma radiation data sets. This work has resulted in the following conclusions:

(1) Comparison of laboratory based χ and ^{40}K gamma radiation data sets from the two sections on the same samples or levels show that these data are well correlated and show good climate cyclicity. This indicates that the χ and gamma radiation data are reflecting the same physical processes, a detrital/eolian terrestrial sediment flux into the marine environment, that is recording climate cyclicity.

(2) Both the χ and ^{40}K data sets yield good power in several Milankovitch climate bands in both the GSSP and the S Sections.

(3) While the GSSP shows good correlations between the χ, GRS, ^{40}K and elemental data sets, the S Section shows poor correlations. This difference is attributed to weathering in the S Section.

(4) Close-interval GRS field measurements in the two sections yield broadly smoothed data sets that are certainly useful in correlating over short distances but appear to result primarily from locally derived bentonites in the sections. This suggests that because of the extreme smoothing due to the large cone of gamma-ray acquisition, such data sets may not be useful for global correlations or for time-series analyses, except in unusual cases.

(5) The highest χ and GRS values are associated with bentonite Beds 69 and 80–82, with some high values in shale samples.

(6) While there is excellent agreement between the χ and ^{40}K gamma radiation data sets in most cases, there are some intervals were the two data sets are not correlated. This is due to local variations in the Fe and K mineralogical effects in samples that show low χ and gamma radiation variability.

(7) Replicate ^{40}K gamma radiation measurements to test the performance level of laboratory instruments are necessary before choosing the sample size and time to be used in data acquisition. Results for the HPGe instrument at LSU used in this study,

indicate that the optimum size and measurement time is at least 10 g for 60 min.

(8) χ field measurement instruments are good for rapid field exploration but appear to suffer from low precision (high scatter) when χ values are low, which is the dominant case for marine sedimentary rocks.

(9) While ferrimagnetic grains are essentially ubiquitous in rocks, even when present these minerals may not influence the χ. Therefore it is recommended that χ-based and not remanence-based measurements be used if a determination of χ in samples is important, when χ is being measured.

In addition, previous work on the C–T GSSP (Ellwood et al., 2008) was expanded and a new Floating Point Time Scale (FPTS) was established for the section using the Milankovitch E1 eccentricity band with ~100 kyr cyclicity (50 kyr half cycles). The sediment accumulation rate estimates (~0.46 cm/kyr) and timing for sediments exposed at the GSSP to accumulate (~2.7 myr) reported here, are similar to other such estimates using different methods.

Acknowledgments

This work was funded in part by a grant to R.E. Crick and B. Ellwood from the National Science Foundation (EAR-9628202) and the Robey Clark Endowment to Geology and Geophysics at LSU. We wish to thank Suzanne Ellwood for her important contribution to this work in designing the sampling method used in collecting our samples, and for her participation in collecting all of the samples used in this study and for help with χ and GRS field measurements. We wish to thank Amber Ellwood for her help in laboratory χ measurement and GRS field measurements.

References

Arthur, M.A., Dean, W.E., Pratt, L.M., 1988. Geochemical and climatic effects of increased marine organic carbon burial at the Cenomanian–Turonian boundary. Nature 335, 714–717.

Barnes, C., Hallam, A., Kaljo, D., Kauffman, E.G., Walliser, O.H., 1996. Global Event Stratigraphy. In: Walliser, O.H. (Ed.), Global Events and Event Stratigraphy. Springer Verlag, pp. 319–333.

Berger, A., Loutre, M.F., Laskar, J., 1992. Stability of the astronomical frequencies over the Earth's history for paleoclimate studies. Science 255, 560–566.

Berrocoso, A.J., MecLeod, K.G., Calvert, S.E., Elorza, J., 2008. Bottom water anoxia, inoceramid colonization, and benthopelagic coupling during black shale deposition on Demerara Rise (Late Cretaceous western tropical North Atlantic). Paleoceanography 23 (PA3212), 1–20. http://dx.doi.org/10.1029/2007PA001545.

Bloemendal, J., deMenocal, P., 1989. Evidence for a change in the periodicity of tropical climate cycles at 2.4 Myr from whole-core magnetic susceptibility measurements. Nature 342, 897–900.

Brook, G.A., Ellwood, B.B., Railsback, L.B., Cowart, J.B., 2006. A 164 ka Record of Environmental Change in the American Southwest from a Carlsbad Cavern Speleothem. Palaeogeography, Palaeoclimatology, Palaeoecology 237, 483–507.

Crick, R.E., Ellwood, B.B., El Hassani, A., Hladil, J., Hrouda, F., Chlupac, I., 2001. Magnetostratigraphy Susceptibility of the Pridoli–Lochkovian (Silurian–Devonian) GSSP (Klonk, Czech Republic) and a Coeval sequence in Anti-Atlas Morocco. Palaeogeography, Palaeoclimatology, Palaeoecology 167, 73–100.

da Silva, A.-C., Boulvain, F., 2002. Sedimentology, magnetic susceptibility and isotopes of a Middle Frasnian carbonate platform: Tailfer Section, Belgium. Facies 46, 89–102.

da Silva, A.-C., Boulvain, F., 2005. Upper Devonian carbonate platform correlations and sea level variations recorded in magnetic susceptibility. Palaeogeography, Palaeoclimatology, Palaeoecology 240, 373–388.

Dettinger, M.D., Ghil, M., Strong, C.M., Weibel, W., Yiou, P., 1995. Software expedites singular-spectrum analysis of noisy time series. EOS. Transactions of the American Geophysical Union 76, 12–21.

Ellwood, B.B., Burkart, B., 1996. Chapter 7: Test of hydrocarbon-induced magnetic patterns in soils: The sanitary landfill as laboratory. In: Schumacher, D., Abrams, M.A. (Eds.), Hydrocarbon migration and its near-surface expression: AAPG Memoir 66, Tulsa, OK, pp. 91–98.

Ellwood, B.B., Chrzanowski, T.H., Hrouda, F., Long, G.J., Buhl, M.L., 1988. Siderite formation in anoxic deep-sea sediments: a synergetic bacterially controlled process with important implications in paleomagnetism. Geology 16, 980–982.

Ellwood, B.B., Crick, R.E., El Hassani, A., 1999. The magnetosusceptibility event and cyclostratigraphy (MSEC) method used in geological correlation of Devonian rocks from Anti-Atlas Morocco. American Association of Petroleum Geologists Bulletin 83, 1119–1134.

Ellwood, B.B., Crick, R.E., El Hassani, A., Benoist, S.L., Young, R.H., 2000. The magnetosusceptibility event and cyclostratigraphy (MSEC) method applied to marine rocks: detrital input versus carbonate productivity. Geology 28, 1134–1138.

Ellwood, B.B., MacDonald, W.D., Wheeler, C., Benoist, S.L., 2003. The K–T Boundary in Oman: Identified Using Magnetic Susceptibility Field Measurements with Geochemical Confirmation. Earth and Planetary Science Letters 206, 529–540.

Ellwood, B.B., Balsam, W.L., Roberts, H.H., 2006. Gulf of Mexico sediment sources and sediment transport trends from magnetic susceptibility measurements of surface samples. Marine Geology 230, 237–248.

Ellwood, B.B., Tomkin, J.H., Ratcliffe, K.T., Wright, M., Kafafy, A.M., 2008. High resolution magnetic susceptibility and geochemistry for the Cenomanian/Turonian boundary GSSP with correlation to time equivalent core. Palaeogeography, Palaeoclimatology, Palaeoecology 261, 105–126.

Ellwood, B.B., Tomkin, J.H., El Hassani, A., Bultynck, P., Brett, C.E., Schindler, E., Feist, R., Bartholomew, A., 2011. A climate-driven model and development of a floating point time scale for the entire Middle Devonian Givetian Stage: A test using magnetostratigraphic susceptibility as a climate proxy. Palaeogeography, Palaeoclimatology, Palaeoecology 304, 85–95.

Elrick, M., Molina–Garza, R., Duncan, R., Snow, L., 2009. C-isotope stratigraphy and paleoenvironmental changes across OAE2 (mid-Cretaceous) from shallow-water platform carbonates of southern Mexico. Earth and Planetary Science Letters 277, 295–306.

Febo, L.A., 2007. Paleoceanography of the Gulf of Papua using multiple geophysical and micropaleontological proxies: Dissertation, Louisiana State University, Baton Rouge, LA., pp. 163. URL: http://etd.lsu.edu/docs/available/etd-11152007-182141/.

Febo, L.A., Ellwood, B.B., Watkins, D.K., 2007. Detrital controls on magnetosusceptibility and cyclostratigraphy records. EOS (Trans. Am. Geophysical Union), AGU Fall Meeting, San Francisco.

Forster, A., Kuypers, M.M.M., Turgeon, S.C., Brumsack, H.-J., Petrizzo, M.R., Sinninghe Damsté, J.S., 2008. The Cenomanian/Turonian oceanic event in the South Atlantic: new insights from a geochemical study of DSDP Site 530A. Palaeogeography, Palaeoclimatology, Palaeoecology 267, 256–283.

Gale, A.S., Voigt, S., Sageman, B.B., Kennedy, W.J., 2008. Eustatic sea-level record for the Cenomanian (Late Cretaceous)—Extension to the Western Interior Basin, USA. Geology 36, 859–862.

Ghil, M., Allen, R.M., Dettinger, M.D., Ide, K., Kondrashov, D., Mann, M.E., Robertson, A., Saunders, A., Tian, Y., Varadi, F., Yiou, P., 2002. Advanced spectral methods for climatic time series. Reviews of Geophysics 40, 3.1–3.41. http://dx.doi.org/10.1029/2000RG000092.

Gradstein, F.M., Ogg, J.G., Schmitz, M.D., Ogg, G.M., 2012. The Geologic Time Scale 2012. Cambridge University Press, England 1144.

Halgedahl, S.L., Jarrard, R.D., Brett, C.E., Allison, P.A., 2009. Geophysical and geological signatures of relative sea level change in the upper Wheeler Formation, Drum Mountains, west-central Utah: a perspective into exceptional preservation of fossils. Palaeogeography, Palaeoclimatology, Palaeoecology 277, 34–56.

Hansen, H.J., Lojen, S., Toft, P., Dolenec, T., Yong, J., Michaelsen, P., Sarkar, A., 1999. Magnetic susceptibility of sediments across some marine and terrestrial Permo-Triassic boundaries. Proceedings of the International Conference "Pangea and the Paleozoic–Mesozoic transiction". China University of Geosciences, Hubei, China, pp. 114–115.

Hladil, J., Gersl, M., Strnad, L., Frana, J., Langrova, A., Spisiak, J., 2006. Stratigraphic variation of complex impurities in platform limestones and possible significance of atmospheric dust: a study with emphasis on gamma-ray spectrometry and magnetic susceptibility outcrop logging (Eifelian–Frasnian, Moravia, Czech Republic). International Journal of Earth Sciences (Geologische Rundschau) 95, 703–723.

Huber, B.T., Leckie, R.M., Norris, R.D., Bralower, T.J., CoBabe, E., 1999. Foraminiferal assemblage and stable isotope change across the Cenomanian–Turonian boundary in the subtropical North Atlantic. Journal of Foraminiferal Research 29, 392–417.

Jarvis, I., Murphy, A.M., Gale, A.S., 2001. Geochemistry of pelagic and hemipelagic carbonates: criteria for identifying systems tracts and sea-level change. Journal of the Geological Society of London 158, 685–696.

Jenkins, G.M., Watts, D.G., 1968. Spectral Analysis and its Applications. Holden–Day, San Francisco (525 pp.).

Jovane, L., Florindo, F., Sprovieri, M., Pälike, H., 2006. Astronomical calibration of the late Eocene/early Oligocene Massignano section (central Italy). Geochemistry, Geophysics, Geosystems 7, Q07012. http://dx.doi.org/10.1029/2005GC001195.

Karlin, R., Levi, S., 1983. Diagenesis of magnetic minerals in recent haemipelagic sediments. Nature 303, 327–330.

Karlin, R., Levi, S., 1985. Geochemical and sedimentological control of the magnetic properties of hemipelagic sediments. Journal of Geophysical Research 90, 10373–10392.

Keller, G., Berner, Z., Adatte, T., Stueben, D., 2004. Cenomanian–Turonian and $\delta^{13}C$, and $\delta^{18}O$, sea level and salinity variations at Pueblo, Colorado. Palaeogeography, Palaeoclimatology, Palaeoecology 211, 19–43.

Kennedy, W.J., Walaszczyk, I., Cobban, W.A., 2005. The Global Boundary Stratotype Section and Point for the base of the Turonian Stage of the Cretaceous: Pueblo, Colorado, U.S.A. Episodes 28, 93–104.

Laskar, J., Robutel, P., Joutel, F., Gastineau, M., Correia, A., Levrard, B., 2004. A long-term numerical solution for the insolation quantities of the Earth. Astronomy and Astrophysics 428, 261–285.

Ogg, J.G., Ogg, G., Gradstein, F.M., 2008. The Concise Geologic Time Scale. Cambridge University Press, England 177.

Parente, M., Frijia, G., Di Lucia, M., Jenkyns, H.C., Woodfine, R.G., Baroncini, F., 2008. Stepwise extinction of larger foraminifers at the Cenomanian–Turonian boundary:

A shallow-water perspective on nutrient fluctuations during Oceanic Anoxic Event 2 (Bonarelli Event). Geology 36, 715–718.
Pearce, T.J., Besly, B.M., Wray, D.S., Wright, D.K., 1999. Chemostratigraphy: a method to improve interwell correlation in barren sequences — a case study using onshore Duckmantian/Stephanian sequences (West Midlands, U.K.). Sedimentary Geology 124, 197–220.
Pearce, T.J., Wray, D.S., Ratcliffe, K.T., Wright, D.K., Moscariello, A., 2005. Chemostratigraphy of the Upper Carboniferous Schooner Formation, southern North Sea. In: Collinson, J.D., Evans, D.J., Holliday, D.W., Jones, N.S. (Eds.), Carboniferous hydrocarbon geology: the southern North Sea and surrounding onshore areas: Yorkshire Geological Society, Occasional Publications series, 7, pp. 147–164.
Pearce, M.A., Jarvis, I., Tocher, B.A., 2009. The Cenomanian–Turonian boundary event, OAE2 and palaeoenvironmental change in epicontinental seas: New insights from the dinocyst and geochemical records. Palaeogeography, Palaeoclimatology, Palaeoecology 280, 207–234.
Ratcliffe, K.T., Wright, A.M., Hallsworth, C., Morton, A., Zaitlin, B.A., Potocki, D., Wray, D.S., 2004. Alternative correlation techniques in the petroleum industry: an example from the (Lower Cretaceous) Basal Quartz, Southern Alberta. Bulletin of the American Association of Petroleum Geologists 88, 1419–1432.
Ratcliffe, K.T., Morton, A., Ritcey, D., Evenchick, C.E., 2008. Whole-rock geochemistry and heavy mineral analysis as exploration tools in the Bowser and Sustut Basins, British Colombia, Canada. Journal of Canadian Petroleum Geology 55, 320–337.
Ratcliffe, K.T., Wright, A.M., Montgomery, P., Palfrey, A., Vonk, A., Vermeulen, J., Barrett, M., 2010. Application of chemostratigraphy to the Mungaroo Formation, the Gorgon Field, offshore Northwest Australia. APPEA Journal 2010 50th Anniversary Issue, pp. 371–388.
Sageman, B.B., Meyers, S.R., Arthur, M.A., 2006. Orbital time scale and new C-isotope record for the Cenomanian–Turonian boundary stratotype. Geology 34, 125–128.
Schlanger, S.O., Jenkyns, H.C., 1976. Cretaceous oceanic anoxic events: Causes and consequences. Geologie en Mijnbouw 55, 179–184.
Seton, M., Gaina, C., Müller, R.D., Heine, C., 2009. Mid-Cretaceous seafloor spreading pulse: Fact or fiction? Geology 37, 687–690.
Shackleton, N.J., McCave, I.N., Weedon, G.P., 1999. Preface. Philosophical Transactions of the Royal Society of London. Series A 357, 1733–1734.
Svendsen, J., Henrik, F., Stollhofen, H., Hartley, N., 2007. Facies discrimination in a mixed fluvio-eolian setting using elemental whole-rock geochemistry—applications for reservoir characterization. Journal of Sedimentary Research 77, 23–33.
Swartzendruber, L.J., 1992. Properties, units and constants in magnetism. Journal of Magnetic Materials 100, 573–575.
Thoa, N.T.K., Huyen, D.T., Ellwood, B.B., Lan, L.T.P., Truong, D.N., 2004. Determination of Permian–Triassic boundary in limestone formations from Northeast of Vietnam by paleontological and MSEC methods. Journal of Sciences of the Earth 26, 222–232.
Thompson, D.J., 1982. Spectrum estimation and harmonic analysis. IEEE Proceedings 70, 1055–1096.
Turgeon, S.C., Creaser, R.A., 2008. Cretaceous oceanic anoxic event 2 triggered by a massive magmatic episode. Nature 454, 323–326.
van Bentum, E.C., Hetzel, A., Brumsack, H.-J., Forster, A., Reichart, G.-J., Sinninghe Damsté, J.S., 2009. Reconstruction of water column anoxia in the equatorial Atlantic during the Cenomanian–Turonian oceanic anoxic event using biomarker and trace element proxies. Palaeogeography, Palaeoclimatology, Palaeoecology 280, 489–498.
Voigt, S., Gale, A.S., Flögel, S., 2004. Midlatitude shelf seas in the Cenomanian–Turonian greenhouse world: Temperature evolution and North Atlantic circulation. Paleoceanography 19 (PA4020), 1–17. http://dx.doi.org/10.1029/2004PA001015.
Voigt, S., Aurag, A., Leis, F., Kaplan, U., 2007. Late Cenomanian to Middle Turonian high-resolution carbon isotope stratigraphy: New data from the Münsterland Cretaceous Basin, Germany. Earth and Planetary Science Letters 253, 196–210.
Weedon, G.P., Jenkyns, H.C., Coe, A.L., Hesselbo, S.P., 1999. Astronomical calibration of the Jurassic time-scale from cyclostratigraphy in British mudrock formations. Philosophical Transactions of the Royal Society London, Series A 357, 1787–1813.
Wright, A.M., Ratcliffe, K.T., Zaitlin, B.A., Wray, D.S., 2010. The application of chemostratigraphic techniques to distinguish compound incised valleys in low-accommodation incised-valley systems in a foreland-basin setting: an example from the Lower Cretaceous Mannville Group and Basal Colorado Sandstone (Colorado Group), Western Canadian Sedimentary Basin. In: Ratcliffe, K.T., Zaitlin, B.A. (Eds.), Modern alternative stratigraphic techniques; theory and case histories: SEPM Special Publication, No. 94, pp. 93–109.